W(h)ither human cardiac and body magnetic resonance at ultrahigh fields? technical advances, practical considerations, applications, and clinical opportunities

Niendorf, T., Paul, K., Oezerdem, C., Graessl, A., Klix, S., Huelnhagen, T., Hezel, F., Rieger, J., Waiczies, H., Frahm, J., Nagel, A.M., Oberacker, E., Winter, L.

Niendorf, T., Paul, K., Oezerdem, C., Graessl, A., Klix, S., Huelnhagen, T., Hezel, F., Rieger, J., Waiczies, H., Frahm, J., Nagel, A.M., Oberacker, E., Winter, L. W(h)ither human cardiac and body magnetic resonance at ultrahigh fields? technical advances, practical considerations, applications, and clinical opportunities. NMR Biomed 29(9): 1173-1197, 2016. doi: 10.1002/nbm.3268

NMR in Biomedicine
2015 FEB 23 (version of record online); 2016 SEP, 29(9): 1173-1197 (final print version)
doi: 10.1002/nbm.3268
Publisher: Wiley-Blackwell

W(h)ither Human Cardiac and Body Magnetic Resonance at Ultrahigh Fields?

Technical Advances, Practical Considerations, Applications, and Clinical Opportunities

Thoralf Niendorf[1,3], Katharina Paul[1], Celal Oezerdem[1], Andreas Graessl[1], Sabrina Klix[1], Till Huelnhagen[1], Fabian Hezel[1], Jan Rieger[2], Helmar Waiczies[2], Jens Frahm[4,5], Armin M. Nagel[6], Eva Oberacker[1] and Lukas Winter[1]

[1)] Berlin Ultrahigh Field Facility (B.U.F.F.), Max-Delbrueck Center for Molecular Medicine, Berlin, Germany

[2)] MRI.TOOLS GmbH, Berlin, Germany

[3)] DZHK (German Centre for Cardiovascular Research), partner site Berlin, Germany

[4)] Biomedizinische NMR Forschungs GmbH am Max-Planck-Institut für biophysikalische Chemie, Göttingen, Germany

[5)] DZHK (German Centre for Cardiovascular Research), partner site Göttingen, Germany

[6)] Medical Physics in Radiology, German Cancer Research Center (DKFZ), Heidelberg, Germany

Address correspondence to:

Thoralf Niendorf,
Berlin Ultrahigh Field Facility (B.U.F.F.)
Max-Delbrueck Center for Molecular Medicine
Robert-Roessle-Strasse 10
13125 Berlin
Germany

phone: +49 030 9604 4505
fax: +49 030 9604 49178
e-mail: thoralf.niendorf@mdc-berlin.de

Short title:

Advances in Ultrahigh Field Cardiac and Body Magnetic Resonance

Key words:
magnetic resonance; MRI; ultrahigh field; cardiovascular imaging; body imaging, heteronuclear MR; MR technology; radio frequency coils

Grant sponsors:

This work was supported (in part, C.O.) by the DZHK (German Centre for Cardiovascular Research) and by the BMBF (German Ministry of Education and Research. This work was funded (in part, A.G.) by the Helmholtz Alliance ICEMED – Imaging and Curing Environmental Metabolic Diseases, through the Initiative and Network Fund of the Helmholtz Association (ICEMED-Project 1210251). L.W. and H.W. received support by the German Federal Ministry of Education and Research ("KMU-innovativ": Medizintechnik MED-373-046).

Word count: 11782

Abstract

Objective: To document and review advances and groundbreaking progress in cardiac and body magnetic resonance (MR) at ultrahigh fields (UHF, $B_0 \geq 7.0$ T) with the goal to attract talent, clinical adopters, collaborations and resources to the biomedical and diagnostic imaging communities.

Methods: This review surveys traits, advantages and challenges of cardiac and body MR at 7.0 T. The considerations run the gamut from technical advances to clinical opportunities. Key concepts, emerging technologies, practical considerations, frontier applications and future directions of UHF body and cardiac MR are provided. Examples of UHF cardiac and body imaging strategies are demonstrated. Their added value over the kindred counterparts at lower fields is explored along with an outline of research promises.

Results: The achievements of cardiac and body UHF-MR are powerful motivator and enabler, since extra speed, signal and imaging capabilities may be invested to overcome the fundamental constraints which continue to hamper traditional cardiac and body MR applications.

Conclusions: If practical obstacles, concomitant physics effects and technical impediments can be overcome in equal measure, sophisticated cardiac and body UHF-MR will help to open the door to new magnetic resonance imaging and spectroscopy approaches for basic research and clinical science; with the lessons learned at 7.0 T being transferred into broad clinical use including diagnostics and therapy guiding at lower fields.

Key words:

magnetic resonance; MRI; ultrahigh field; cardiovascular imaging; body imaging, heteronuclear MR; MR technology; radio frequency coils

List of Abbreviations

λ	wavelength
ε	permittivity
σ	electrical conductivity
^{1}H	hydrogen protons
^{23}Na MRI	sodium magnetic resonance imaging
^{31}P MR	phosphorous magnetic resonance
AMI	acute myocardial infarction
ATP	adenosine triphosphate
B_0	main magnetic field strengths
B_1^+	electromagnetic transmission field
BMI	body mass index
BMR	body magnetic resonance
CEM43°C	cumulative equivalent minutes at 43 degrees celsius
CAI	coronary artery imaging
CMR	cardiac magnetic resonance
CP-like	circularly polarized-like
CPU	central processing unit
DREAM	dual refocusing echo acquisition mode
DWI	diffusion-weighted imaging
D_2O	deuterium oxide
ECG	electrocardiogram
EMF	electromagnetic fields
EPI	echo planar imaging
f	frequency
FA	flip angle
FLASH	fast low angle shot
FOV	field of view
FSE	fast spin-echo
GPC	glycerophosphocholine
GPE	glycerophosphoethanolamine
IEC	international electrotechnical commission
MALSE	magnetic field alert sensor
MHD	magneto-hydrodynamic
MIP	maximum intensity projection
MPS	monocyte phagocytic system
MRA	magnetic resonance angiography
MRC	magnetic resonance cholangiography
MRS	magnetic resonance spectroscopy
NA	number of averages
Na^+	sodium
NaCl	sodium chloride
PC	phosphocholine
PCr	phosphocreatine
PD	proton density
PE	phosphoethanolamine
PINS	power independent number of slices
Pi1 and Pi2	two phosphate peaks
pTX	parallel transmission
R_1	longitudinal relaxivity
R_2	transversal relaxivity
RF	radio frequency
RFPA	radio frequency power amplifiers
RX	radio frequency reception

SAR	specific absorption rate
ShMOLLI	shortened modified look locker inversion
SD	standard deviation
SNR	signal-to-noise ratio
SSFP	steady state free precession
TX	radio frequency transmission
T_1	longitudinal relaxation time
TE_{01} mode	transverse electric mode 01
T_2	transversal relaxation time
T_2*	effective transversal relaxation time
TE	echo time
TIAMO	time-interleaved acquisition of modes
TR	repetition time
UHF-MR	ultrahigh field magnetic resonance
VOPS	virtual observation points

Graphical Abstract

W(h)ither Human Cardiac and Body Magnetic Resonance at Ultrahigh Fields

Thoralf Niendorf, PhD, Katharina Paul, Dipl.Phys., Celal Oezerdem, Dipl.-Ing., Andreas Graessl, Dipl.-Ing., Sabrina Klix, BSc, Till Huelnhagen, Dipl.-Ing., Fabian Hezel, Dr.rer.med., Jan Rieger, MSc, Helmar Waiczies, PhD, Jens Frahm, PhD, Armin M. Nagel, PhD, Eva Oberacker, Dipl.-Phys. and Lukas Winter; PhD

Short abstract

This work documents and reviews advances and progress in cardiac and body magnetic resonance technology at ultrahigh fields and its application in forefront research and in early clinical applications. The achievements of ultrahigh field cardiac and body magnetic resonance are shown to be a powerful motivator and enabler, since the extra speed, signal and imaging capabilities may be invested to overcome the fundamental constraints which continue to hamper traditional cardiac and body magnetic resonance applications at lower magnetic field strengths.

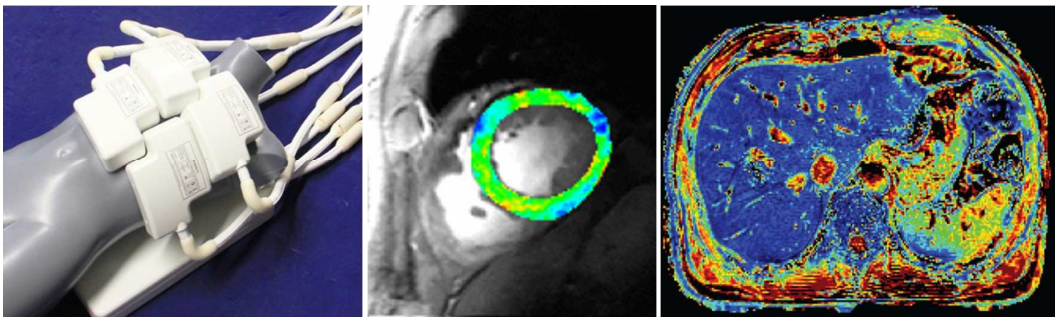

Introduction

The growing number of reports referring to technology transfer and explorations into body and cardiovascular applications is an inherent testament to the advancements of magnetic resonance (MR) at ultrahigh magnetic field strengths ($B_0 \geq 7.0$ T, $f \geq 298$ MHz). Pioneering explorations into ultrahigh field (UHF) body MR (BMR) document the progress in liver, renal, abdominal, pelvic and prostate imaging and spectroscopy (1-24). Early applications of UHF cardiac MR (CMR) manifest the advances for imaging and spectroscopy of the heart and the large vessels (25-59). These technical and pilot studies respond to unsolved problems and unmet needs of today's clinical body/cardiac MR. These developments are fueled by the signal-to-noise ratio (SNR) advantage inherent to higher magnetic field strengths and are driven by explorations into novel MR technology.

The progress is heartening and creates the legitimate temptation to sing the praise of UHF-BMR/CMR. Transferring UHF-BMR and UHF-CMR into the clinic remains a major challenge though (32) since the advantages are sometimes hampered by a number of concomitant physics related phenomena and by practical impediments. It is no secret that these obstacles bear the potential to spoil the benefits of UHF-CMR/BMR. Although reports from clinical early adopters of 7.0 T BMR/CMR remain largely anecdotal at this point, momentum is gathering for broader applications oriented feasibility studies and for clinical studies, which will be enabled by increasingly robust and streamlined hardware and software platforms.

Recognizing the technical advances and clinical opportunities of UHF-BMR/CMR together with the need for broader clinical studies this review is an attempt to make the (bio)medical and diagnostic imaging communities aware of this productive ferment, so as to engage the interest of potential clinical adopters, to inspire collaborations across disciplinary boundaries and to attract basic scientists, engineers, hardware professionals, translational researchers, applied scientists and new entrants into the field; with the goal to advance the capabilities of UHF-

BMR/CMR by fostering explorations into the many remaining unresolved problems and technical obstacles. In the sections that follow, examples of enabling UHF-BMR/CMR technology and their applications are provided. Encouraging developments into multiple channel radiofrequency (RF) concepts are reviewed. Advances in imaging methodology and progress in RF pulse design are discussed. Early and frontier applications of BMR/CMR at 7T are surveyed together with the clinical opportunities for high spatial resolution MR, parametric mapping, MR angiography and real time imaging; all being facilitated by the traits of UHF-MR. Liver, renal and prostate UHF-BMR applications are presented. Heteronuclear UHF-BMR/CMR applications are explored including sodium MR and phosphorous MR. Practical considerations of UHF-BMR/CMR are outlined. The subjective acceptance during UHF-BMR/CMR examinations is discussed. Insights into RF heating induced by conductive stents and implants along with RF power deposition considerations are provided. Current trends in UHF-BMR/CMR are considered together with their clinical implications. A concluding section ventures a glance beyond the horizon and explores future directions. Of course, ultrahigh field BMR/CMR is an area of vigorous ongoing research, and many potentially valuable developments will receive only brief mention here.

Technical Solutions for Ultrahigh Field Body and Cardiac MR

Enabling Radio Frequency Coil Technology

At ultrahigh fields the crux of the matter is that the wavelength becomes sufficiently short versus the size of the upper torso, abdomen and pelvis. As deep-lying organs surrounded by the lung, stomach, bowels and other inhomogeneous tissue structures within the comparatively large volume of the thorax, abdomen and pelvis, the anatomy targeted in CMR and BMR is particularly susceptible to non-uniformities in the RF transmission field (B_1^+). These detrimental B_1^+ phenomena can cause shading, massive signal drop-off or even signal void and hence bear the potential to offset the benefits of UHF-BMR/CMR due to non-diagnostic image quality.

To address this obstruction for broader clinical studies a plethora of reports eloquently refers to the development of enabling RF technology tailored for BMR and CMR at 7.0 T. In fact, the momentary non-uniformities in the transmission fields in the thorax and abdomen are generally so significant that the use of traditional birdcage body coils at 298 MHz become elusive if not prohibitive. This need has inspired explorations into novel RF technology including cardiac and body optimized multi-channel coil array configurations. Research directions include (i) local transceiver (TX/RX) arrays and (ii) multi-channel transmission arrays in conjunction with multi-channel local receive arrays.

Arguably, the wide spectrum of BMR/CMR applications is ranging from large volume imaging to localized spectroscopic probing which renders the design of a single optimal many-element RF coil configuration elusive. Obviously, the selected RF coil design should first of all meet the requirements of patient safety, patient comfort and ease of clinical use to harmonize the technical specifications with the clinical needs. This includes light weight, flexibility, capability to accommodate multiple body habitus and anatomical variants, a modular and multi-dimensional arrangement of

coil elements or building blocks together with a sensitive region large enough to cover the target anatomy in the upper torso, abdomen and pelvis (32).

Multi-channel RF coil designs tailored for UHF-BMR/CMR involve rigid, flexible and modular configurations. The gestation process revealed a trend towards a larger number of transmit and receive elements (31,35,37-39,53) to improve anatomic coverage and to advance the capabilities for transmission field shaping (60). Pioneering developments made good use of building blocks that include stripline elements (6,25,26,61,62), elecrical dipoles (46,62-65), dielectric resonant antennas (55) and loop elements (31,35,37-39,53), with the number of independent elements ranging from two to thirty two.

Loop element based CMR/BMR optimized 7.0 T transceiver configurations were reported for an 4-channel TX/RX design that is equipped with two anterior and two posterior elements (Figure 1a) (35). An alternative loop array comprises eight TX/RX channels split into five anterior and three posterior elements (Figure 1b) (37). Both configurations make use of a one-dimensional arrangement of the elements. This setup constrains the degree of freedom for transmission field optimization and for parallel imaging. A two-dimensional arrangement of loop elements uses sixteen TX/RX channels with the elements being distributed to eight anterior and eight posterior elements; both arranged in a 2 x 4 array (Figure 1c) (39). This approach was extended to a more sophisticated modular 32 channel TX/RX array shown in Figure 1d (53). This configuration comprises four planar (posterior section) and four modestly shaped (anterior section) modules (53); each module being fitted with four independent transceiver loop elements (2 x 2 array).

Various stripline element based 7.0 T transceiver configurations were proposed for cardiac and body UHF-MR. In a pioneering 8 element transverse electromagnetic field (TEM) transceiver array design each element was independently connected to a dedicated RF power amplifier (25). Other stripline array configurations run flexible designs consisting of a pair of four (Figure 2a) or eight stripline elements, one placed

anterior and the other posterior to the torso (26,61). Another practical solution comprising an eight channel stripline transceive array (Figure 2b) that uses sophisticated automated tuning with piezoelectric actuators was accomplished (54).

Electric dipoles have been shown to be suitable for CMR and BMR at 7.0 T including deep seated targets such as the prostate and the pelvis (46,63). Electric dipoles run the trait of a linearly polarized current pattern, where RF energy is directed perpendicular to the dipole along the Poynting vector to the subject resulting in a symmetrical, rather uniform excitation field with increased depth penetration (63). Early implementations include straight dipole elements (63). To enable efficient power transmission from dipole antennae the length of the antenna needs to be adjusted to the transmission frequency so that the antenna size can be as long as 35-50 cm for a straight, self-resonant half wavelength dipole antenna at 297MHz. This geometry is suitable for large volume body MRI at 7.0 T but imposes a constraint (i) for the design of many element, two-dimensional transceiver arrays confined to cardiac fields of view and (ii) for parallel imaging along all standard and multi-oblique cardiac views. The need for densely packed multichannel transceiver coil arrays tailored for UHF-BMR/CMR inspired explorations into electric dipole configurations that comprise 8 or 16 bow tie antenna building blocks as shown in Figure 1e,f. Each of the building blocks contains a bow tie shaped $\lambda/2$-dipole antenna immersed in D_2O (46) which is an MR inactive molecule with a permittivity of $\varepsilon \approx 81$ at 298 MHz. This approach helps to shorten the effective antenna length. To establish a CMR/BMR array of 16 independent TX/RX channels eight bow tie antenna building blocks were combined to form an anterior and a posterior coil section, each in a 4 x 2 array (Figure 1f).

Improvements in the compactness of dipole antenna arrays were also accomplished by incorporating lumped element inductors, by using fractionated dipoles (Figure 2c) or by employing meander structures (66-68). The requirements of UHF-BMR/CMR along with ultimate intrinsic SNR and current pattern considerations inspired alternative dipole antenna designs. One important development is bent

electric dipoles (69). Other configurations include circular dipoles, which consist of a circular conductor with a feed point on one side and a gap on the other (70). Recently proposed dipole antenna variants include folded dipoles (71).

Another conceptually very much appealing building block design is the dielectric resonant antenna fabricated with high permittivity, low loss ceramics (55). These building blocks are designed to operate in the TE_{01} mode at 298 MHz (55). This resonance mode dictates the disc geometry which for example resulted in a diameter of 86 mm and a height of 39 mm for $BaSrTiO_3$ resonators with a relative permittivity of 165 (55). Inductive coupling using a small non-resonant coupling loop per resonator was applied for impedance matching and for coupling energy into the ceramic resonator. To form an 8 element transceiver array four building blocks were placed on top of the anterior chest while 4 building blocks were positioned posterior to the upper torso (Figure 2d).

To summarize, stripline elements, dielectric resonant antennae, loop elements and electric dipoles are valuable building blocks for local transceiver coil configurations customized for BMR and CMR at 7.0 T. To this end ultimate intrinsic signal-to-noise ratio (UISNR) considerations outlined that loop- and dipole current patterns contribute equally to UISNR at 7.0 T (72,73). For field strengths of $B_0 \geq 9.4$ T current patterns are dominated by linear (dipole type) current patterns (72,73), which provides motivation for shifting the weight to dipoles versus loop and stripline elements.

Multi-Channel RF Chain

To translate the capabilities of multi-channel RF coil configurations into practical value advances in MR systems hardware abounded. Contemporary UHF-MR systems architecture supports multi-channel transmit arrays to be driven in two modes, using (i) an array of independent feeding RF power amplifiers (RFPA) with exquisite control of phase, amplitude or even complete RF waveforms for all

individual channels or (ii) a single feeding RFPA. For the single feeding RFPA regime the amplifier output is commonly split into fixed-intensity signals using RF power splitters. Phase adjustments for individual coil elements or groups of coil elements are accomplished with phase-shifting networks or coaxial cables. This setup provides a practical solution which can be made readily available for a large number of MR sites. In today's research implementations RFPA's with up to 16 kW peak power are used for the single feeding RFPA mode. State of the art multi feeding RFPA implementations support up to 16 RF amplifiers each providing up to 2 kW adjustable RF output power. This setup provides software driven control over phase and amplitude by modulating the applied input signal. Moreover it enables sophisticated parallel transmission of independent RF waveforms to every channel. On the journey to a broader range of UHF-BMR/CMR applications it is beneficial if RF coil configurations provide flexibility which supports single feeding as well as multiple feeding RFPA regimes without major changes in cabling and other components (53).

Advances in Imaging Methodology

Advances in imaging methodology comprise two main categories for UHF-BMR/CMR: (i) novel approaches for transmission field mapping and (ii) new technologies for transmission field shaping.

The knowledge of the spatial B_1^+ distribution generated by coil arrays is pivotal for UHF-BMR/CMR to manage transmission fields across the target region including signal excitation, signal refocusing, and magnetization preparation. B_1^+ mapping approaches commonly used are mainly magnitude-based and are generally confined to the ratios or the fit of signal intensity images (74-81). For this purpose sets of images are acquired using either two flip angles (75-77), identical flip angles but different repetition times (TR) (79), variable flip angles (78,80) or signals from spin-echoes and stimulated-echoes (74), as well as signals from gradient-echoes and stimulated-echoes (82). It should be noted that B_1^+ mapping is not a need limited to

transceiver arrays tailored for ^{1}H UHF-MR. For instance B_1^+ mapping has been applied to ^{23}Na MRI to support quantification of sodium tissue content (83).

Many of the B_1^+ mapping techniques rely on the knowledge of the steady state magnetization B_1^+ (75). This makes large volume coverage flip angle mapping time consuming due to the speed constraints dictated by the need for rather long repetition times (TR > 5 T_1) to avoid T_1 saturation effects. Also, the competing constraints of cardiac and respiratory motion limit the viable window of data acquisition so that B_1^+ mapping of the heart and body is commonly limited to single slice breath-held acquisitions. To address the anatomic coverage and speed constraints a B_1^+ mapping approach was proposed which is based on a magnetization prepared transient gradient-echo sequence and that facilitates sub-second acquisitions (82). The speed gain renders the dual refocusing echo acquisition mode (DREAM) suitable for large volume coverage multi-slice acquisitions within clinically acceptable breath-hold durations. B_1^+ mapping with DREAM was shown to be adjuvant for liver imaging which benefits from the improvements in flip angle accuracy and transmission field uniformity over the target volume (84). The propensity of DREAM to blood flow is a remaining concern for cardiovascular and body B_1^+ mapping. To offset the flow sensitivity of DREAM a Motion-Sensitized Driven-Equilibrium magnetization preparation was used which showed ample suppression of blood signal in the cardiac chambers and in large vessels (85).

Phase-based techniques present an alternative for B_1^+ mapping, and were reported to be more accurate versus magnitude-based methods for the low flip angle regime (86). These methods commonly make use of a composite or off-resonance RF-pulse to encode the spatial B_1^+ information into the phase of the magnetization vector. Most phase based methods, however, make use of non-selective pulses for volume excitation in conjunction with 3D imaging schemes (87-89). This approach results in relatively long acquisition times that often exceed clinically acceptable breath-hold periods along with a pronounced susceptibility for

respiratory motion artifacts. Realizing these limitations, the feasibility of cardiac gated, single breath-hold B_1^+ mapping has been demonstrated (90) using a 2D phase-based Bloch-Siegert approach (91). The reduction of the duration of the Fermi pulse allowed for short TR which enabled scan times accommodated by a single breath hold. It is a remaining issue, that phase based B_1^+ mapping might not be exclusively governed by the phase accrual induced by the composite RF pulse but might also reflect phase contributions due to blood flow and cardiac motion. Preliminary results did not show major changes in the calculated flip angle at the blood/myocardium interface and hence indicate that blood flow related phase contributions might be minor (90).

Notwithstanding the advances in B_1^+ mapping methodology transmission field mapping of individual coil elements at 7.0 T has been primarily established for head imaging (92-94) but remains a challenge for UHF-BMR/CMR due to depth penetration constraints and susceptibility artifacts. To cope with this challenge B_1^+ profiles are often derived from numerical electromagnetic field (EMF) simulations (39,53,95). For this purpose the transmit phases for each coil element are adjusted using iterative algorithms to improve transmission field homogeneity in a region of interest encompassing the heart or the abdomen using a human voxel model (96). To ensure that the relative B_1^+ distributions of the individual coil elements derived from the EMF simulations accord with reality it is essential that EMF simulations are validated against MR measurements using phantoms filled with a dielectric liquid that resemble the dielectric properties of the target organ/tissue as outlined in (Figure 3). While the single feeding RFPA mode provides a practical solution it comes with the caveat that subject specific B_1^+ shimming is not supported. Hence the applicable range of body geometries and body mass indices (BMI) is centered around the reference subject or the human voxel model used for B_1^+ optimization. Notwithstanding this drawback clinically acceptable image quality can be obtained for UHF-CMR for a common range of BMI's without the need of patient-specific adjustments (38,39,53), bringing this technology closer to product development and broader clinical use.

Based upon *a priori* acquired B_1^+ maps derived for all individual transmit channels of an coil array B_1^+ shimming can be used to reduce RF non-uniformities across the torso using the degrees of freedom of multi-channel transmission to shape the transmission field for UHF-CMR/BMR. Figure 4 shows an example for B_1^+ uniformity improvements across a 4 chamber view of the heart using a 32 channel TX/RX coil in conjunction with B^{1+} shimming that makes use of (i) a B_1^+ optimized phase setting using 32 elements, (ii) a phase setting per building block each comprising 4 elements and (iii) a circularly polarized-like (CP-like) phase setting for all elements (53).

The acquisition of two or more time-interleaved images recorded with complementary RF excitation modes is an extension of static RF shimming in the single feeding RFPA regime (97). This methodology helps to mitigate signal voids due to B_1^+ non-uniformities by combining the B_1^+ spatial RF excitation patterns (98). The enhanced B_1^+ uniformity comes with a scan time or signal-to-noise ratio drawback. This spatio-temporal resolution penalty can be offset by combined reconstruction of virtual coil elements in conjunction with parallel imaging techniques (97).

Arguably, the single RFPA B_1^+ shimming regime is static and offers limited capabilities if more sophisticated and dynamic B_1^+ adjustments are needed to support cascades of B_1^+ shimming stages including slice-by-slice specific B_1^+ shimming, subject specific B_1^+ trimming or magnetization preparation modules driven by B_1^+ efficiency requirements versus imaging modules governed by B_1^+uniformity needs. Dynamic shimming is the forte of the multi feeding RFPA's mode in conjunction with sophisticated pulse sequence developments which support cascades of dynamic B_1^+ shimming stages that balance the needs of preparation modules common in body and cardiac imaging such as inversion, fat suppression or blood suppression, pencil beam excitation across the diaphragm for navigator gated respiratory motion compensation and rapid imaging modules. Frontier BMR/CMR implementations of dynamic B_1^+ shimming at 7.0 T include 2D CINE imaging (99), coronary MR angiography (100), renal MR angiography (12), 4D flow MR angiography of the entire

aorta (101) and arterial spin labeling perfusion imaging of the kidneys (102) which demonstrated improved excitation efficiency, increased SNR of myocardium and blood, enhanced blood/myocardium contrast or helped to balance the B_1^+ uniformity with B_1^+ efficiency (103).

Progress in RF Pulse Design

Multi-channel transmission (104-107) using spoke RF pulses presents a major breakthrough for pulse sequence developments tailored for UHF-BMR/CMR (49). A juxtaposition of the two-spoke approach with B_1^+ shimming revealed an enhanced excitation fidelity or a reduced RF pulse energy for the two-spoke technique (49). This benefit holds the promise to be instrumental for a broader range of CMR applications, including uniform excitation for parametric mapping used for tissue characterization. Current pulse designs for two-spoke parallel transmission RF pulses make use of a single set of B_1^+ /B_0 maps though. This approach may not be suitable for subsequent scans acquired at another respiratory phase because of organ displacement, which might induce severe excitation profile degradation. To address this issue, a tailored parallel transmission RF pulse design which is immune for respiration induced B_1^+ /B_0 variations has been recently proposed (58). In analogy to the CMR implementation the two-spoke approach can be exploited to mitigate B_1^+ inhomogeneity in target regions encompassing the pelvis, the abdomen or the liver (15). Multi-band spokes pulses afford simultaneous multi-slice acquisitions with enhanced flip angle homogeneity but minimal increase in integrated and peak radiofrequency power (108).

On the RF pulse design side adiabatic RF pulses and composite RF pulses offer a practical solution to offset the B_1^+ uniformity constraints. These RF pulses provide nearly constant flip angles over a wide B_1^+ range, with a common lower limit of approximately 60% of the expected B_1^+. This advantage comes at the cost of RF power deposition. This issue is pronounced for fast spin-echo based imaging

techniques which exhibit an increased propensity to B_1^+ inhomogeneities. The power deposition constraint manifests itself in limited spatial coverage by allowing only few slices for fast spin-echo imaging. To relax this caveat adiabatic RF pulses are commonly prolonged with pulse durations exceeding 10 ms to reduce peak RF power (17). Obviously, the long inter-echo times put an extra burden onto the point spread function of fast spin-echo imaging which can inadvertently diminish the usefulness of the spatial resolution enhancements of UHF-BMR/CMR. Slice accelerated acquisition schemes using power independent number of slices (PINS) RF pulses which perform spatially periodic excitation and refocussing provide means for relaxing RF power deposition in spin-echo based imaging at 7.0 T (109).

Adiabatic RF pulses were also used in spectrally selective adiabatic RF inversion based fat suppression with the goal to enhance contrast between coronary lumen blood pool and epicardial fat (30). Hyperbolic-secant RF pulses were employed to form a saturation pulse train optimized for first pass myocardial perfusion MRI at 7.0 T (51).

To deal with respiratory motion in BMR/CMR prospective navigator gating and tracking using 2D selective pencil beam excitation is another area of activity for RF pulse developments (29). For CMR at 7.0 T the heart/lung interface rather than the diaphragm is used for navigator localization (29). For this purpose the duration of the 2D selective pencil beam navigator RF pulse was significantly decreased versus protocols established at 3.0 T to master susceptibility artifacts at the heart/lung interface (29).

Applications and Clinical Opportunities

Cardiac Chamber Quantification

Early UHF-CMR applications demonstrated the usefulness of 2D CINE spoiled gradient-echo imaging (FLASH) for cardiac chamber quantification of the left (28,34,36) and right ventricle (44) at 7.0 T. 2D CINE FLASH provides high quality images with uniform signal intensity distribution and high blood/myocardium contrast over the entire heart as demonstrated in Figure 5. Cardiac chamber quantification at 7.0 T agrees closely with LV and RV parameters derived at 1.5 T (34).

The baseline SNR gain at 7.0 T can be translated into spatial resolution enhancements versus the kindred counterparts at lower field strengths. Figure 6 surveys four chamber and short axis views of the heart obtained with a standardized CMR protocol (110,111) and with an enhanced spatial resolution. The latter protocol reduces the voxel size from 19.4 mm^3 to 1.6 mm^3, equivalent to a twelve-fold improvement in the spatial resolution versus a standardized clinical CMR protocol. This fidelity approaches an effective anatomical spatial resolution – voxel size per anatomy – which resembles that demonstrated for animal models (112). The overall image quality and improvements in spatial resolution enabled the visualization of fine subtle anatomic structures including the compact layer of the free right ventricular wall and the remaining trabecular layer. Pericardium, mitral and tricuspid valves and their associated papillary muscles, and trabeculae are identifiable. For the short axis views a standard deviation of the signal intensity over the myocardium of approximately 20% was observed.

A recent implementation demonstrated the applicability of slice selective two-spoke parallel transmit RF pulses in cardiac 2D CINE imaging at 7T (49). For this purpose cardiac gated, breath-held B_1^+ multi-channel calibration maps and ΔB_0 maps were acquired to guide the amplitude and phase modulated RF pulse design for each channel. With the two-spokes approach the B_1^+ field was found to be

improved significantly for the posterior region of a four chamber view of the heart including the atria and the large vessels (49). With a two spoke pulse setting transmitter voltage/RF pulse energy could be increased by 22%/50% to obtain higher blood/myocardium contrast without exceeding the RF power deposition limits (49).

First Pass Myocardial Perfusion Imaging

Clinical CMR assessment of ischemic heart disease includes rapid first-pass contrast agent enhanced myocardial perfusion MRI (111). Numerous saturation-recovery-based perfusion techniques have been proposed to capture first-pass kinetics with one- or two-heart-beat temporal resolution**.** Saturation methods established at lower fields are suboptimal for myocardial perfusion imaging at 7.0 T (51). To address this issue a novel saturation pulse train consisting of four hyperbolic-secant (HS8) radiofrequency pulses was proposed for effective saturation of myocardium at 7.0 T (51). This approach facilitated an average saturation efficiency of 97.8% in native myocardium and afforded the first series of human first-pass myocardial perfusion images at 7.0 T (51). The ability to produce exquisite in-plane spatial resolution at 7.0 T may offer greater diagnostic value for myocardial perfusion assessment and supports an extension of the perfusion assessment to the right ventricle. With sufficient acceleration and imaging speed, perfusion imaging is on the verge for 3D whole heart coverage acquisitions (113) which might be furthered by the traits of UHF-MR.

Myocardial T_2* Mapping

The ability to probe for changes in tissue oxygenation using T_2^* sensitized imaging/mapping offers the potential to address some of the spatial and temporal resolution constraints of conventional first pass perfusion imaging and holds the promise to obviate the need for exogenous contrast agents. For T_2* mapping at 7.0 T a reasonable B_0 uniformity across the heart is key so that susceptibility weighting is not

dominated by macroscopic B_0 field inhomogeneities but rather by microscopic B_0 susceptibility gradients (42). A mean peak-to-peak B_0 difference of approximately 65 Hz was found across the left ventricle (42), which compares well with 3.0 T (114) and 1.5 T studies (115). For myocardial anterior, anterolateral and inferoseptal segments a mean in-plane B_0 gradient of approximately 3 Hz/mm was observed. With this B_0 uniformity high spatial resolution myocardial T_2^* mapping at 7.0 T is feasible (42,48) as demonstrated in Figure 7. The longest mean T_2^* values were found for the anterior (T_2^*=17.3 ms), anteroseptal (T_2^*=16.8 ms) and inferoseptal (T_2^*=16.3 ms) segments. Septal segments showed the lowest spatial variation in T_2^*, which is similar to that reported for 1.5 T and 3.0 T (48). The inferior (T_2^*=12.0 ms) and inferior lateral (T_2^*=11.4 ms) wall yielded lowest T_2^* values with the spatial variation being significantly pronounced versus 1.5 T and 3.0 T (48). The 7.0 T setup used facilitated a spatial resolution as good as (1.1x1.1x2.5) mm^3, which helped to reduce intravoxel dephasing along the slice direction (42).

Detailing magnetic field strength dependence revealed that myocardial T_2^* decreases linearly with B_0 with the mean global T_2^* of healthy myocardium being approximately 14 ms at 7.0 T versus 27 ms at 3.0 T (116) and approximately 37 ms at 1.5 T (117). This makes the susceptibility effect due to (patho)physiology of interest more pronounced, so that T_2^* mapping at 7.0 T might be beneficial to address some of the BOLD sensitivity constraints reported for the assessment of regional myocardial oxygenation changes in the presence of coronary artery stenosis (118). The recent progress in *in vivo* histology and in fiber orientation tracking using T_2^* weighted and susceptibility weighted MR (119-121) suggests that the linear relationship between T_2^* and B_0 might provide means to gain a better insight into the myocardial microstructure. Since the susceptibility effects depend on the tilt angle between blood filled capillaries and the external magnetic field strength (115,122-124) T_2^* mapping at 7.0 T might contribute to explorations into visualization of myocardial

fibers, into the examination of helical angulation of myocardial fibers or into the assessment of fibrotic tissue and other kinds of microstructural tissue changes.

To avoid T_2* quantification errors due to signal modulations induced by fat-water phase shift, echo times where fat and water are in-phase are commonly used for T_2* mapping (125). This translates into inter-echo times of ΔTE=2.2 ms at 3.0 T and ΔTE=4.4 ms at 1.5 T. Consequently it is elusive to study temporal changes in T_2* across the cardiac cycle at 1.5T and 3.0T due to scan time constraints which are prohibitive for CINE T_2* mapping covering the cardiac cycle. At 7.0 T ΔTE governed by the fat-water shift is 1.02 ms, which facilitates CINE T_2* mapping customized for T_2* monitoring across the cardiac cycle (Figure 7) (42). The improved temporal resolution of T_2* mapping at 7.0 T provides means for monitoring externally controlled variations of blood oxygenation including short periods of hypoxia and hyperoxia test stimuli (126,127).

Myocardial T_1 Mapping

Myocardial tissue characterization using T_1-weighted late gadolinium enhancement imaging is of proven clinical value for the assessment of ischemic heart diseases but also for non-ischemic myocardial diseases (111). T_1-weighted imaging is qualitative and subjective though, which demands advancements towards myocardial T_1 mapping (128-130). At 7.0 T increased RF transmit power and improved B_0 shimming play complementary roles for myocardial T_1 mapping which requires careful transmission field shaping and B_0 shimming. This requirement can be managed if quantification of and correction for imperfect inversion is applied (47). For this purpose an adiabatic inversion pulse tailored for use in the heart in conjunction with a ShMOLLI variant was employed (47). Subject averaged inversion efficiencies ranging from -0.79 to -0.83 (perfect inversion would provide -1) were accomplished across myocardial segments (47). T_1 of normal myocardium has been reported to be (1925±48) ms at 7.0 T (47) versus (1166±60) ms at 3.0 T (131) and (721±37) ms at 1.5 T

(130). The prolonged T_1 relaxation times at 7.0 T provide an enhanced blood/myocardium contrast superior to 1.5 T which afforded a revival of spoiled gradient-echo imaging techniques at 7.0 T. Slice selective variable flip angle techniques provide an alternative for rapid parametric T_1 mapping (132). This approach obviates the need for inversion recovery preparation while being fast enough to meet the speed requirements of cardiac MR.

Fat Water Imaging

Fat-water separated cardiac imaging provides a sensitive means of detecting intramyocardial fat, characterizing fibro-fatty infiltration, characterizing fatty tumors, and delineating epicardial and/or pericardial fat. Multi-echo Dixon approaches utilizing iterative decomposition have been shown to provide robust fat-water separation even in the presence of large field inhomogeneities (133). Equipped with this technology fat-water separated imaging at 7.0 T has been demonstrated for cardiac and body applications (134-136).

Coronary Artery Imaging

CAI remains technically challenging due to small vessel size, vessel tortuosity, and physiological motion (137,138). UHF-CAI studies using non-contrast gradient-echo imaging techniques suggested that image quality did already approach that achieved for CAI at 3.0 T (29,30,50). Coronary vessel sharpness at 7.0 T was found to be improved versus 3.0 T (30). The early studies focused primarily on the right coronary. To afford appropriate coverage of all main coronary arteries the capabilities of dynamic B_1^+ shimming were exploited (100). The capabilities of UHF-CAI were furthered by employing high spatial resolution CAI (Figure 8a) (50). For this approach coronary vessel edge sharpness was found to be superior to the boarder sharpness accomplished in state-of-the-art CAI at 3.0 T. Visible vessel length and vessel diameter obtained at 7.0 T were competitive with 3.0 T (50).

Traditional frequency selective fat saturation techniques used in CAI might suffer from large static field variations at 7.0 T which may cause non-uniform and imperfect fat-suppression over the target region; an effect which bears the risk to obscure the delineation of coronary arteries. Here fat-water separated imaging holds the promise to substitute conventional preparatory fat saturation techniques (Figure 8b). This approach also promises to offset some of the RF power deposition constraints which come with conventional saturation recovery based fat saturation that makes use of large flip angles.

Vascular Imaging

MR angiography (MRA) of the large vessels is a common cardiovascular MR application. MRA stands to benefit from UHF-MR. The SNR gain can be used to counter the noise amplification caused by acceleration techniques employed to meet the high spatiotemporal resolution requirements of MRA. Potential applications include large volume coverage, time-resolved phase velocity MRA (4D flow) which is an emerging technique for studying the flow pattern or wall shear stress in large vessels. The feasibility of aortic 4D flow at 7T was recently demonstrated (56). For this purpose a prospectively gated 4D flow sequence was applied. This approach provided a SNR enhancement of 2.2/3.7 versus 3.0 T/1.5 T for non-contrast enhanced acquisitions in the descending aorta (56). Another 4D flow MRA implementation at 7.0 T made good use of dynamically applied B_1^+ shimming toggling a setting tailored for the navigator used for respiratory gating and the imaging module (101).

Perhaps UHF-MR forms another important enabling factor to transform the baseline SNR advantage into improved spatiotemporal resolution of contrast enhanced MRA. To this end an SNR gain for contrast enhanced versus non-contrast enhanced 4D flow MRA was reported to be approximately 1.4 at 7.0 T which was found to be in accordance to 3.0 T and 1.5 T observations (56). Research continues to examine the impact of prolonged T_1 relaxation times and altered R_1 and R_2 relaxivity

of clinically approved gadolinium(III) chelate based contrast media on the blood/background tissue contrast at 7.0 T. These studies include the assessment of contrast agent doses required to accomplish maximal available contrast enhancement (139,140).

Black Blood Imaging

Transfer of fast spin-echo based black blood imaging to 7.0 T is of high relevance for advancing the capabilities of UHF-CMR for explorations into cardiac morphology and myocardial tissue characterization. FSE imaging at 7.0 T presents a special challenge due to the train of high peak RF power refocusing pulses ($\alpha \leq 180°$). Notwithstanding its utility for improving B_1^+ uniformity in UHF-FSE imaging, recent studies on using adiabatic pulses for UHF-FSE reported long inter echo times of up to 15 ms; an approach which does not meet the CMR requirements.

The feasibility of cardiac FSE imaging at 7.0 T using an eight channel transceiver array of bowtie antennas (Figure 1e) is demonstrated in Figure 8c. For this purpose a spatial resolution of (0.9 x 0.9 x 4.0) mm^3 was applied, which represents an order of magnitude improvement versus standardized protocols of today's clinical CMR practice (111). The blood suppression inherent to FSE works well in most regions of the heart. Only slow flowing blood in areas close to the endocardium remains visible. The refinement of black blood preparation modules – including double inversion recovery preparation – tailored for 7.0 T is anticipated to further FSE image quality at 7.0 T. Here a modest diffusion weighting could provide a valuable alternative for spoiling remaining signal induced by slow flowing blood. Figure 8c also indicates that the dynamic range of FSE image contrast at 7.0 T is dominated by subcutaneous fat signal despite the applied spectral preparation pulse, which requires further efforts into fat suppression techniques. Alternatively, reduced field of view acquisition can be exploited to exclude subcutaneous fat of the chest wall from the field of view. The application of double echo FSE techniques, which afford a

simultaneous combination of different image contrasts provides opportunities to advance the capabilities of UHF black blood imaging (141). Generating dual contrast simultaneously within one acquisition offers substantial scan time reduction. This is of benefit in a clinical scenario where multiple parameters/contrasts are assessed. Moreover, simultaneous acquisition of multiple contrasts obviates the need for slice co-registration when combining multiple series of images with anatomical (T_2 or PD) and functional (DWI) contrast, which would be beneficial for CMR dealing with physiological motion. The use of self-calibrated parallel imaging techniques tailored for FSE imaging presents another opportunity to extend the capabilities of black blood imaging at 7.0 T (142). For this purpose the full echo of coherent FSE needs to be decomposed into two parities, which can be independently phase encoded (i) using regular sampling to derive coil sensitivity profiles and (ii) k-space undersampling for accelerated FSE acquisitions (142). One practical implication is that the speed gain of self-calibrated FSE would help to reduce examination times while improving both operator convenience and patient comfort.

Real Time Imaging

Breath-held 2D CINE acquisitions segmented over regular 10-16 heartbeats are the clinical standard for LV structure and function assessment. Yet, the traditional approach is limited by physiological (e.g. cardiac arrhythmias) constraints, which might cause inappropriate diagnostic information. Free breathing real time cardiac MRI achieves diagnostic quality in a single heartbeat (143) and bears the potential to change the landscape of cardiac diagnostics (144-146). These developments will afford an improved clinical accuracy and efficacy of CMR. The accelerated imaging capabilities and the anatomic coverage of multi-channel bow tie antenna arrays (Figure 1e,f) supported free breathing real time imaging of the heart and of the aorta at 7.0 T (Figure 9). The spatial resolution of (1.2 x 1.2 x 6.0) mm^3 and the frame rate of 30 frames per second fully meet if not excel the requirements of standardized left

ventricular structure and function assessment protocols used in today's CMR practice (111). The real time FLASH images of the aorta demonstrated the extended anatomic coverage of the 16 channel bow tie antenna array along the head-feet direction including details of the liver and the spine without B_1^+ signal voids (Figure 9). Real time imaging also provides opportunities for high spatiotemporal resolution UHF-BMR including tracking abdominal and pelvic moving pattern and for assessing small bowel disease (147,148).

Renal Imaging

The potential spatial resolution advantage of UHF-BMR would benefit the evaluation of patients with renal insufficiency, renal tissue hypoperfusion/hypoxia, effects of iodinated x-ray contrast media, or acute kidney injury and its progression to chronic kidney disease, and preoperative evaluation of renal vasculature and anatomy (126,127,149,150). The feasibility of renal MRI at 7T was demonstrated at an early stage of the development process (5). At this stage it was concluded that T_1 weighted gradient-echo MRI provides best image quality and excellent conspicuity of the non-enhanced vasculature which is beneficial for time of flight MRA (Figure 10). The feasibility of dynamic contrast enhanced T_1-weighted renal imaging (Figure 10) was demonstrated (4). Image quality obtained for T_2 weighted FSE imaging was strongly impaired because of signal inhomogeneities.

The evaluation of the potential of high spatial resolution MRA of the renal vasculature using contrast enhanced (4) and non-contrast enhanced (7) techniques at 7.0 showed enhanced vessel delineation and vessel conspicuity. First pass perfusion renal MRA revealed an improvement in vessel delineation versus non-contrast acquisitions (11).

In more sophisticated implementations of renal MRA at 7.0 T dynamically applied B_1^+ shimming solutions were incorporated into a non-contrast enhanced renal MRA technique that makes use of two B_1^+-shim sets (12): one customized for B_1^+

efficiency maximization to drive contrast preparation and another one tailored for uniform low flip angle imaging (12). This approach supports high resolution imaging of the renal vasculature derived from low flip angle gradient-echo acquisitions.

Numerous (pre)clinical studies underscored the growing scope of T_2* sensitized renal MRI and its value for the noninvasive assessment of renal oxygenation and perfusion (150). To further the capabilities of renal imaging it is compelling to advance high spatial resolution imaging and T_2^* mapping of the kidney at 7.0 T.

Liver Imaging

Liver imaging constitutes a growing fraction of clinical MRI including the assessment of focal liver lesions, diffuse liver disease and liver vessel pathologies. A typical liver exam consists of T_2-weighted imaging with and without fat saturation, and T_1-weighted gradient-echo imaging prior to and following administration of contrast media. Since UHF-BMR becomes more widespread, its advantages can be potentially exploited to drive the spatial resolution into the sub-millimeter range and to enhance the liver vessel/parenchyma contrast. T_1 weighted imaging of the liver was shown to support whole liver coverage (Figure 11a) and high details of subtle liver structures without the need of contrast agent application (Figure 11b) (21). Besides the gallbladder and the great vessels, capillaries in the dimension of half a millimeter of diameter were clearly identifiable due to the superb spatial resolution of (0.3x0.3x2.5) mm^3 (Figure 11c) which is superior to that commonly achieved in clinical settings at 1.5 T and 3.0 T (135,136). Contrast-enhanced T_1-weighted MR cholangiography (MRC) using 3D gradient-echo techniques facilitated a uniform depiction of the intra- and extrahepatic biliary tract at 7.0 T with the depiction of the intrahepatic bile ducts being superior to MRC at 3.0 T (19). The use of multi-spoke slice-selective parallel transmit RF pulses would be beneficial for mitigating B_1^+ inhomogeneities observed for liver MRI at 7T (15). Unlike B_1^+ field distribution, B_0 uniformity was found to be

acceptable as indicated by rather uniform T_2* across the liver (Figure 11d) (135) with T_2*≈10 ms for the parenchyma and T_2*≈10 ms for the large liver vessels.

Liver fat/water imaging was reported to be feasible with fat and water being correctly classified across the full field of view (135). Providing MR-based liver fat and volume could be utilized as endpoints in patients with non-alcoholic fatty liver disease or obesity. It is challenging though, to incorporate fat-water separation into FSE commonly used for diagnostic T_2-weighted liver and abdominal imaging which requires uniform fat suppression. To address this issue a slice-selective gradient reversal technique was applied, which provided uniform fat suppression with moderate tissue signal loss of approximately 20% (18). This approach was combined with the TIAMO technique (97) which facilitated delineation between fat and bright liquids in single-shot FSE (18). The progress in FSE imaging of the liver at 7.0 T opens opportunities for diffusion weighted imaging of the liver free of geometric distortion, which is elusive for DWI-EPI because of susceptibility induced distortions. Working towards this direction would provide means for evaluating hepatic fibrosis.

Prostate Imaging

Indications for MRI of the prostate include the evaluation of prostate cancer and MRI guided prostate biopsy (151-154). The sensitivity gain at 7.0 T holds the promise to obviate the use of endorectal coils for prostate MRI. Early explorations into prostate MRI at 7.0 T demonstrated high quality images facilitated by transceiver arrays in conjunction with patient specific local B_1^+ shimming (2). With this signal homogeneity and spatial resolution clear delineation of anatomical features in the prostate and surrounding structures including the neurovascular bundle, the rectum, the urethra, the transition zone, the peripheral zone and the fibromuscular tissue was achieved (2). Careful examination of the B_1^+ efficiency and B_1^+ uniformity of an endorectal coil and an eight-element microstrip transceiver array at 7.0 T suggested the use of the microstrip array for T_1- and T_2 weighted prostate imaging, whereas the

endorectal coil was considered to be the best choice for spectroscopic studies (6). Further advancements in B_1^+ efficiency and uniformity together with a four-fold reduction in local RF power deposition and a 40% SNR increase in the center of the prostate were accomplished by adding an extra stripline element to the conventional endorectal coil (9). The lessons learned from these developments culminated in high quality T_2 weighted FSE imaging of the human prostate using an external transceive body array coil (17) in healthy subjects and in patients with prostate cancer (Figure 12) (17). This pioneering study demonstrated that prostate tumors diagnosed or confirmed with MR-guided biopsy or prostatectomy were well visualized with 7.0 T MRI (17).

Sodium MRI

Sodium MRI (^{23}Na MRI) is an emerging approach for gaining better insights into cellular metabolism with a broad spectrum of biomedical imaging research applications (155). Previous studies eloquently reported credible data on ^{23}Na MRI of the heart and demonstrated that ^{23}Na-MRI is suitable for the detection and assessment of acute and chronic heart disease (156). The rapidly decaying ^{23}Na signal and the low sensitivity of ^{23}Na MRI versus ^{1}H MR constitute a challenge for clinical ^{23}Na CMR. Once clinically feasible, sodium MRI holds the promise to become a valuable diagnostic tool for classifying viable from non-viable tissue in ischemic infarct patients. Recognizing the sensitivity gain and yet unimpaired transmission field homogeneity (43) due to the comparably low ^{23}Na resonance frequency which is close to ^{1}H MRI at 1.5 T it is conceptually appealing to pursue cardiac ^{23}Na MRI at 7.0 T at clinically acceptable acquisition times. To approach this goal a local four-element transceiver RF surface coil customized for cardiac ^{23}Na MR at 7.0 T was employed to derive ^{23}Na images of the heart (Figure 13) with a resolution of (6x 6 x 6) mm^3 using a density-adapted 3D radial acquisition technique (157). These efforts also demonstrated that the sensitivity gain at 7.0 T enables CINE ^{23}Na imaging of the

beating heart using a temporal resolution of 100 ms supported by retrospectively gated, density-adapted 3D projection reconstruction (158).

Beyond viability imaging ^{23}Na MR promises to change the landscape for monitoring Na^+ disposition in the body which is important in cardiovascular research. A high dietary salt (sodium chloride) intake and the metabolic syndrome are the driving forces for risk factors of the cardiovascular epidemic. Sodium metabolism is closely linked mechanistically to the metabolic syndrome. Na^+ can be bound to proteoglycans that are particularly abundant in the skin. Earlier determinations of skin and muscle Na^+ concentrations in humans were reduced to chemical analysis following excision of material. Such an approach is not clinically acceptable. This state-of-affairs suggests assessment of sodium content using UHF-MR. The spatial resolution enhancements over 3.0 T setups revealed for the first time the enormous Na^+ content of the human skin with a millimeter in-plane spatial resolution and a <11% intra-subject variability (83,159). It stands to reason that the combination of high resolution ^1H UHF-MR and sophicticated ^{23}Na MR image reconstruction techniques that include prior knowledge from ^1H MRI will enable even higher spatial resolutions for ^{23}Na MR (160).

^{23}Na MRI has been also employed to examine renal sodium content at 7.0 T (Figure 13). These efforts showed that renal ^{23}Na concentration increases from the cortex to medullary pyramid direction (20). ^{23}Na T_2* relaxation times were reported to differ between the cortex (17.9±0.8 ms) and medulla (20.6±1.0 ms) (20). This affords the use of clinical imaging protocols built on gradient-echo techniques which would be beneficial for translating renal ^{23}Na MRI into broader in vivo studies at 7.0 T.

The preliminary results suggest that ^{23}Na MRI at 7.0 T can help to unlock questions regarding Na^+ balance and Na^+ storage functions of kidney, skin and muscle with the ultimate goal to provide imaging means for diagnostics and for guiding treatment decisions in cardiovascular and metabolic diseases.

Phosphorous MR

Phosphorus MR affords in vivo insights into the energy metabolism and is an ideal candidate to benefit from the sensitivity gain and improved frequency dispersion at higher fields. To demonstrate the sensitivity gain, careful juxtaposition between cardiac ^{31}P-MRS at 7.0 T and 3.0 T was conducted (52). These pioneering studies revealed marked superiority of cardiac ^{31}P spectra at 7T relative to 3T (Figure 14). SNR improvements of 2.8 for PCr (52) together with a reduced standard deviation for the PCr/ATP ratio were observed. This gain resulted in an enhanced quantification accuracy at 7.0 T. Myocardial ^{31}P T_1 relaxation times are shorter at 7.0 T versus 3.0 T. These improvements could permit scan time reductions versus 3.0 T and might eventually allow metabolic probing of dynamic processes. For all these reasons it was concluded that 7.0 T will become the field strength of choice for cardiac ^{31}P MR spectroscopy tailored for probing myocardial energy metabolism (52).

Probing phosphorylated metabolites with ^{31}P MRS can be also used for prostate cancer characterization at 7.0 T (13). ^{31}P spectroscopic imaging using an endorectal coil together with adiabatic excitation enabled the acquisition of phosphorous spectra covering the entire prostate with a spatial resolution of 4 cm^3 in 18 min (10) or of 5.1 cm^3 in approximately 9 min (Figure 14). This achievement supported the detection of phosphocholine, phosphoethanolamine and inorganic phosphate that could serve as MR based biomarker for prostate cancer diagnostics. An exploratory study involving 15 patients with biopsy-confirmed prostate cancer showed distinct features of phospholipid metabolites in the prostate gland and its surrounding structures (22). However, no differences in the phosphorous metabolite ratios were found between prostate cancer and normal-appearing prostate tissue (22). These observations warrant optimization of ^{31}P MRS technology including RF coil developments, evaluation of T_1 relaxation times and detailing the impact of the Nuclear Overhauser Effect of phosphorus-containing metabolites at 7.0 T (23).

Practical Considerations

Ancillary Devices

Physiological motion and flow constraints dictate the viable window for data acquisition in CMR/BMR. Cardiac motion is commonly dealt with using electrocardiographic (ECG) gating techniques. ECG being an electrical measurement is corrupted by interference with electromagnetic fields and by magneto-hydrodynamic (MHD) effects (40). As UHF-MR becomes more widespread, the significance of artifact sensitivity of ECG recordings increases and with it the motivation for a practical hardware solution. To this end an MR-stethoscope which builds on the phonocardiogram and which is immune to interferences with electromagnetic fields has been proposed and evaluated for the pursuit of robust and safe cardiac gated/triggered UHF-CMR (27,33,161,162).

BMR and CMR applications involve the injection of contrast media. Contrast agent application is most effective and reproducible using a power injector versus manual injection. While many power injectors customized for MR are approved for use at 1.5 T and 3.0 T, assessment and certification of safety, functionality, flow rate, volume and timing fidelity remains an open task at 7.0 T. The electro-mechanical injector components positioned in the 7.0 T environment are of particular safety concern since the fringe field is stronger and larger versus a clinical 1.5 T or 3.0 T system. Hence it is prudent to mount the powerhead on the wall inside of the scanner room. This approach might come at the cost of an increased length of the supply lines over a 1.5 T and 3.0 T setup. This issue can be fixed through recalibration of the power injector.

Subjective Acceptance of UHF-BMR/CMR examinations

On the journey to broader clinical UHF-BMR/CMR applications it is of relevance to scrutinize how UHF-CMR examinations are tolerated by subjects. Practical concerns evoked by the physical size and mere length of today's 7.0 T MR scanner and the paucity of data about ergonomic constraints, (dis)comfort and sensory side effects are driving the notion that UHF-BMR/CMR constitutes a challenge for subject tolerance of 7.0 T examinations *per se*. Realizing the lack of data a recent study examined the subjective acceptance during UHF-CMR in a cohort of 165 healthy subjects (59). A questionnaire was used to examine the participant's experience prior, during and after the UHF-CMR examination. Transient muscular contraction was documented in 12.7% of the questionnaires (59). Muscular contraction was reported to occur only during periods of scanning with the magnetic field gradients being rapidly switched. Dizziness during the study was reported by 12.7% of the subjects (59). Taste of metal was documented by 10.1% of the study population. Light flashes were outlined by 3.6% of the entire cohort. 13% of the subjects reported side effects/observations which were not explicitly listed in the questionnaire but covered by the question about other side effects and observations (59). No severe side effects as vomiting or syncope after scanning occurred. No increase in heart rate was observed during the UHF-CMR exam versus the baseline clinical examination. To summarize, UHF-CMR examinations are well tolerated by healthy subjects. Broader observational and multi-center studies including patient cohorts with cardiac diseases are required to gain further insights into the subjective acceptance of UHF-CMR examinations.

RF Power Deposition Considerations

Radiofrequency pulses used in MR applications at low and high magnetic fields deposit RF power in tissue, which can be described by the specific absorption rate (SAR):

$$SAR = \frac{\sigma|\vec{E}|^2}{\rho} \quad (1)$$

with the tissue conductivity σ, the root mean square of the electric field $\vec{E}$ and the tissue density ρ. Excessive SAR levels might lead to elevated temperature levels making a careful SAR evaluation mandatory to confirm compliance with the RF power deposition limits given by the IEC standard 60601-2-33:2010 Ed.3 (163) for safe operation of transmit RF coils tailored for UHF-CMR/BMR (163). For this purpose it is circumspect that the safety assessment, the implemented safety measures, the technical documentation and the risk management file for the RF coil are evaluated and made available for implementation in clinical studies following a review and conformity declaration - confirming compliance with the relevant sections of IEC 60601-2-33:2010 Ed.3 and IEC 60601-1:2005 Ed.3. - issued by an independent notified body rather than solely conducting an in-house assessment. In-house procedures make it challenging to comply with a standard since they may vary among institutions, depend on the different level of local expertise, might be compromised by the use of not clearly defined reference values and arbitrary tolerances for key parameters governing RF safety and last but not least are not independent. A notified body is an accredited test laboratory that is independent from manufacturer or distributor and that has been approved by an independent third party to perform tests within a defined test scope for medical devices and hence is entitled to examine whether a product or procedure complies with the requirements of a certain standard or an equivalent standard document.

The IEC 60601-2-33:2010 Ed.3 technical standard defines limits for whole body average SAR (normal mode: 2.0 W/kg, 1st level controlled mode: 4.0 W/kg), which is used for large volume body RF coils commonly used for transmission at 1.5T and 3.0T. RF power deposition of local transceiver RF coil arrays used for UHF-BMR/CMR is limited by a more restrictive local SAR of 20W/kg for the trunk in 1st level controlled mode. This restriction implies (i) that the applicable RF power based on local SAR limits is lower than based on whole body or partial body SAR (164,165) and (ii) that more

power has to be applied in order to reach the same flip angle. In addition electrical conductivity is frequency dependent and increases for UHF-MR. This leads to a direct SAR increase as seen from equation 1 and an indirect SAR increase due to lower absolute B_1^+ per input power resulting from higher transmission losses in tissue.

At UHF-MR the wavelength becomes sufficiently short versus the upper torso/abdomen/pelvis which affects the *E* field distribution inside the body and offsets some of the SAR predictions governed by (166):

$$SAR \propto \frac{B_1^2 B_0^2 \tau_{RF}}{m_i TR} \quad (2)$$

RF power deposition is substantially affected by the geometry of the upper torso, by positioning of the RF coil with respect to the torso and the heart, by the RF coil design, by the number of RF transmission channels as well as by the RF driving conditions. Here EMF simulations are essential to provide an insight into the local SAR distribution. Figure 15 illustrates the $B_1^+/\sqrt{kW}/\sqrt{Max\ local\ SAR_{10g}}$ distribution for a cardiac optimized four channel TX/RX array for field strengths ranging from 1.5 T to 14 T. For this purpose the TX/RX array was placed onto the anterior and posterior upper torso of the human voxel model "Duke" (96). For this configuration a lower B_1^+ is achieved for the given local SAR values when moving to higher frequencies. Consequently, a higher RF power deposition is needed to achieve the same flip angle at higher fields. For the setup simulated a SAR increase by a factor of 13.7 was observed for the mid-ventricular septum when moving from 1.5 T to 7.0 T. In comparison, the same myocardial region showed a factor of 3.5 SAR increase when moving from 7.0 T to 14.0 T. For an apical region a SAR increase of factor 8.1 was derived when moving from 1.5 T to 7.0 T and factor of approximately 2.2 was deduced for a B_0 increase from 7.0 T to 14.0 T. The increase in local SAR to achieve the same flip angle is not as pronounced as reported for a single loop cardiac coil (167). This underlines that local SAR depends on the geometry of the

torso/abdomen/pelvis, on the position of the coil with respect to target anatomy, on the RF coil design, on the number of RF transmission channels as well as on the RF driving conditions.

A change in amplitude and phase of each individual transmit channel – commonly used for B_1^+ shimming (1) or parallel transmission (104-107) - may induce significant alterations in local SAR. This behavior generates a need for explorations into concepts for SAR characterization of multi-channel transmission which is relatively new territory. While commercial configurations of multi-channel transmission at 3.0 T are already CE marked and FDA cleared multi-channel transmission configurations at 7.0 T are still investigational devices. This constitutes a major road blocker *en route* to a broader range of UHF-BMR/CMR parallel transmission applications since the primary responsibility for safe use is shifted by the MR manufacturers to the end-users, which creates an asymmetry since it constitutes a subtly but importantly different situation than for "cleared" devices, where this primary responsibility falls to the manufacturers. This asymmetry provides stimulation to the imaging community to throw further intellectual weight behind the solution of the remaining issues. To achieve this goal, strategic research driven by joint efforts of thought leaders from industry, scientists, and clinicians should be devoted to the development of enhanced practical solutions for SAR assessment of multi-transmit configurations. In this light patient safety concepts and algorithms were recently proposed for SAR characterization of multi-channel transmission including EMF simulations using human anatomical models to pre-calculate the electric field distributions of each individual channel (168-170). While being a valuable approach its main limitations are twofold: (i) SAR assessment is based exclusively on human voxel model simulations which may or may not reflect the specific situation of the given subject and (ii) the concept does not contain any provisions for RF waveforms deviating from those included in the calculations due to hardware infidelities or hardware malfunction. In this context a novel, comprehensive RF safety strategy for parallel transmission MR was recently put forward (171). The

proposed approach allows (i) SAR prediction prior to the scan and (ii) SAR supervision during the scan and hence provides means for offsetting SAR overestimation while still meeting the requirements of RF safety (171). For this purpose the comprehensive strategy comprises three stages: (i) SAR prediction using preprocessed numerical simulation data obtained for human body models derived from fater-water separated MRI of heathy volunteers positioned in supine position with the arms parallel to the torso; (ii) a preparation phase, where active decoupling and load compensation are used to ensure the predicted SAR matches the actual SAR applied to the subject; and (iii) supervision during the scan (171). The latter ensures that global and local SAR limits are not exceeded and that the RF waveforms applied are correct as predicted (171).

On-the-fly SAR calculations including determination of momentary RF amplitudes and phases during the scan, real-time calculation of local SAR maxima and interruption of RF transmission in case SAR limits are exceeded constitutes a challenge. To address this issue several methods that significantly reduce the complexity without restriction to particular radiofrequency excitations were proposed (172-176). In a particular implementation it was demonstrated that by compressing complete body models into limited sets of matrices it is sufficient to consider only so-called Virtual Observation Points (VOPs) and still obtain an adequate, conservative estimation of the maximum local SAR (173). The VOPS approach affords substantial processing time savings for maximum local SAR evaluation and hence holds the promise to support online SAR assessment using pre-calculated electric fields of any arbitrary TX array configuration tailored for UHF-BMR/CMR. Ideally, the models used for simulations of electric fields to be delivered to the VOPS interface should involve subject specific geometry and tissue composition (177) resulting in individualized body SAR models that include conductive implants and devices.

Although SAR is key for RF safety evaluations, temperature distribution - which is the cause of tissue damage based on RF heating - doesn't follow SAR in a

straightforward manner (164). Thermoregulation and heat transfer inside the body (i.e. blood vessels) need to be considered while moving towards a more realistic scenario. Ongoing research focusses already on temperature modeling instead of SAR models, suggesting a thermal tissue damage threshold CEM43 known from thermal therapies (178,179). Here realistic thermal modelling based on electromagnetic field simulations and MR thermometry is essential to assess thermal distributions *in vivo* (180,181). These explorations will help to advance towards enhanced MR safety assessment for UHF-BMR/CMR CMR. This development is expected to include a drive towards controlled E-field steering and targeted SAR reduction technologies in electrically conductive implants, catheters and guide wires using parallel transmission to create excitations that induce minimal RF current in elongated conductors (182,183). An open minded look reveals that UHF-CMR parallel transmission technology perhaps forms an enabling platform to advance interventional CMR applications at 7.0 by using an MR antenna array to deliberately focus RF power in a controlled way (46). In this context potential applications could include (i) targeted RF guided drug release and image guided monitoring (184), (ii) localized contrast agent release and tracking or (ii) stem cell delivery to the myocardium afforded by local RF heating. One could even conduct a gedankenexperiment where targeted RF heating driven by multi-transmit UHF-MR technology is utilized in thermal therapies or even used for RF ablation versus today's invasive intracardiac catheter ablation.

Radiofrequency Heating of Conductive Devices

En route to broader clinical UHF-BMR/CMR studies it is essential to gain a better insight into the interaction of passive conducting implants with RF fields. Considering an ever increasing population of patients with a history of stent implantation, detailing the interaction of stents with RF fields is of profound relevance for the advancement of UHF-BMR/CMR. This is not an easy task because of the many RF coil

and stent configurations available, yet becomes even more relevant when moving to many element transceiver arrays or even to large volume coils covering major sections of the body.

At UHF-MR the RF wavelength (λ) in myocardial tissue and blood is sufficiently short (λ~12cm) to induce resonance effects at $\lambda/4$ - $\lambda/2$ (185) in coronary stents with a length of up to ~4cm, a dimension common in clinical practice (186). EMF simulations and RF heating experiments showed that temperature increase due to coronary stents does not exceed baseline RF heating if IEC standards for local and global SAR limits are strictly obeyed (41). While being very important these early studies did not employ a setup which resembles a clinical scenario (41). The need for RF heating assessment at $B_0 \geq 7.0$ T also prompted valuable research into RF induced heating of metallic arterial stents (187). The conclusions drawn are valuable but constrained to the very specific experimental setup used.

Recognizing the opportunities for broader clinical UHF-MR studies RF induced heating of coronary stents was examined at 7.0 T (57,188). For this purpose EMF simulations were performed for a broad range of coronary stent configurations to detail electric fields and local SAR as a function of stent diameter, stent length, stent position with respect to the RF transmission source and stent orientation versus the E-field (57,188). To translate these results to arbitrary coronary stent geometries, arbitrary stent positions and arbitrary RF coil configurations an analytical approach for the assessment of EM fields induced in coronary stents was proposed. SAR_{1g} induced by a stent ($SAR_{1g\ stent}$) can be described by:

$$\max(SAR_{1g\ stent}) = f(diameter, length, orientation) \cdot SAR_{1g\ baseline} \quad (3)$$

with $SAR_{1g\ baseline}$ being the local SAR_{1g} at the assumed stent position without the presence of a stent (57). Figure 16b shows an example of the dependence of induced stent SAR_{1g} on stent length and stent orientation versus the E-field vector.

The analytical approach provides a fast way to estimate induced stent SAR levels. EMF simulations performed with a stent integrated in a human voxel model prove to be very time consuming. This is a particular practical obstacle if many-element RF TX/RX arrays and a set of phase settings mimicking B_1^+-shimming or other parallel transmit applications are included. Benchmarking the analytical approach versus EMF simulations showed a good conservative estimation of induced SAR_{1g} peak levels. A practical example is shown in Figure 16 using an 8 channel bow tie antenna RF coil array optimized for CMR at 7.0 T (Figure 1e). EMF simulations including the stent consumed >2 hours CPU and GPU time per phase setting (not including RF shim field combining and SAR calculations) while the analytical approach can be calculated in real-time. This example underscores the value of the proposed analytical approach for obeying regulatory RF power limits (163). The analytical approach is conceptually translatable to other implant configurations and can be conveniently incorporated into state-of-the art SAR prediction concepts (174,189) to provide SAR estimations induced by coronary stents and other conductive implants for arbitrary RF pulses used for transmission field shimming (2,49) or parallel transmission (105,106). To generalize, this approach provides a novel metric or design criteria for RF coils. E.g. to design RF coils (i) with low SAR levels in the vicinity of the stent or (ii) with SAR levels during the presence of the stent which do not exceed SAR levels without the presence of the stent (57).

Looking Beyond the Horizon

While today's lion's share of UHF-MR examinations covers brain and neuroscience applications, cardiac and body MR are other fields that can benefit from UHF-MR. The eye-opening quality of recent anatomical and functional images, have created excitement in the (bio)medical and diagnostic imaging communities and have served as a driving force for application developments which culminated in the breadth and detail outlined in this review. This progress is no great surprise, but a number of challenges remain. These unsolved problems should not be hidden under the carpet, but rather act as a surface marker thanks to contributions made by the many forward-thinking researchers, clinician scientists and clinicians. This faith attracts resources, fosters collaborations across the banks of what sometimes appears like a wide river, and invites talent. All putting further weight behind solving the conundrum governed by the physics and engineering, with the ultimate goal to harmonize development of novel imaging technology tailored for BMR/CMR with added clinical value, simplicity and ease of use. Meanwhile, the pace of discovery is heartening and a powerful motivator to transfer the lessons learned from UHF-BMR/CMR research into the clinical scenario. These efforts are fueled by the quest for advancing the capabilities of diagnostic MRI, today. A story worth following since the implications feed into a broad spectrum of MR physics, biomedical engineering, radiology, cardiology, internal medicine, oncology, nephrology, and other related fields of basic research and clinical science (190-193). Moreover, the benefits of 7.0 T BMR/CMR innovations will be more being seen at 3.0 T, where the suboptimal copy and paste approach to protocol migration from 1.5T is being supplanted by the sort of application-targeted redesign which is essential for UHF-CMR/BMR.

An open minded look reveals that the field of UHF-BMR/CMR is in a creative state of flux. It is too early in the exploration stage to make ultimate statements though. Technological advances spurred by the low wave length regime have already earned UHF-BMR/CMR the moniker of being a steam engine for innovation

along with the recognition of being advanced UHF-MR applications. The requirements of UHF-BMR/CMR are likely to pave the way for further advances in MR technology and MR systems design. With appropriate multi transmit systems that offer more than 16 TX channels each providing at least 4 kW peak power, an optimistically-inclined scientist might envisage the implementation of high density transceiver arrays with 64 and more elements with the ultimate goal to break ground for a many element upper torso or even a body coil array. This vision continues to motivate new research on integrated multi-channel transmission systems (194), on RF coil design together with explorations into ideal current patterns yielding optimal signal-to-noise-ratio for UHF-BMR/CMR (72). It is also compelling to embark into the development of high density, multiple-channel on-coil transmit arrays which would help to reduce the losses in the RF chain (195). The enlarged spectral resolution along with the sensitivity gain stands to reason to boost 7.0 T MR of a broad spectrum of metabolically relevant nuclei including ^{19}F, ^{13}C, ^{17}O, ^{31}P, ^{23}Na, ^{39}K and ^{35}Cl (196-200). This research will drive explorations into metabolic MR and nanomolecular MR probing for which RF coil innovations is to be expected. Perhaps another development is the move toward CMR/BMR using reduced field of views zoomed into the target anatomy enabled by spatially selective excitation techniques which put the capabilities of parallel transmission technology to good use. Elimination of the information redundancy intrinsic to today's BMR/CMR applications would change the imaging landscape and would help to offset the complexity of today's BMR/CMR exams.

It is no secret that the future of UHF-BMR/CMR will not end at 7.0 T and that the field is moving apace into this direction. On the MR physics side the field strives to extend activities designed to master MR electrodynamics at fields of $B_0 \geq 7.0$ T by progressing numerical simulations. The first pioneering reports on EMF simulations dealing with B_1^+, SAR and temperature distribution for cardiac MR at 10.5 T, 11.7 T or even 14.0 T have been outlined in this review or were released recently (201). On the experimental side the recent progress of probing the local concentrations of fluorine,

sodium, potassium and chlorine at 7.0 T provide convincing reasons for wide bore magnets with $B_0 \geq 7.0$ T which spurred the installation of a 10.5 T whole-body MR system suitable for cardiac and body imaging (201). Alongside this progress there is intriguing news on potential future developments outlined in a report of the National Research Council dealing with high magnetic field science and its application(202). This report forwarded a call for a 20.0 Tesla wide bore MR system, a technical development inspired by the recent progress at 7.0 T, by the early experience with small animal MR at 21.1 T (203) as well as by the lessons learned from the design and safety evaluation of superconducting 13.0 T magnet outserts with a 50 cm bore size retrofitted with a 12 T resistive insert to form a 25.0 T hybrid magnet tailored for structure research (204). Arguably, ^{1}H MR at 20.0 T might be elusive in the first run. Yet, the frequencies of x-nuclei at 20.0 T are below the ^{1}H resonance frequency at 7.0 T, with the exception of ^{31}P and ^{19}F. This makes technology established for ^{1}H MR at 7.0 T ideal candidates to be perfected and fine-tuned for hetero-nuclear BMR/CMR MR at 20.0 T. For example the sensitivity gain at 20.0 T is expected to reduce scan times for ^{31}P and ^{23} Na by a factor of 8 versus today's 7.0 T capabilities. While this is, for the moment, merely a vision, it promises sodium MR with a sub-millimeter spatial resolution in 5-10 min scan time, and offers the potential for probing the heart with ^{31}P spectroscopy in clinically acceptable scan times versus today's groundbreaking studies using scan durations of approximately 2 hours. Also, recognizing the pace and momentum of UHF-MR, the MR vendors committed that there is no U-turn on the Tesla road. In fact they are now driving with full throttle to setup the next generation of whole body 7.0 T magnets. Thitherto UHF-BMR/CMR techniques remain in a state of creative flux and productive engagement in this area continues to drive further developments.

Acknowledgements

The authors wish to acknowledge the members of the Berlin Ultrahigh Field Facility (B.U.F.F.), Berlin, Germany; the members of the MR group at the Medical Metrology Department, Physikalisch-Technische Bundesanstalt, Berlin, Germany; the working group for Cardiac Magnetic Resonance, Charite', Berlin, Germany; Sebastian Aussenhofer, C. J. Gorter Center for High Field Magnetic Resonance, Leiden University Medical Center, Leiden, Maurice M. Bizino and Hildo Lamb, Department of Radiology, Leiden University Medical Center, Leiden, The Netherlands; Stefan Haneder, Institute of Clinical Radiology and Nuclear Medicine, University Medical Center Mannheim, Heidelberg University, Heidelberg, Germany; Alexander Raaijmakers, Department of Radiotherapy, University Medical Centre Utrecht, Utrecht, The Netherlands; Matthew D. Robson and Christopher Rodgers, Radcliffe Department of Medicine, University of Oxford, Oxford, UK; Tom W. J. Scheenen, Department of Radiology, Radboud University Medical Centre, Nijmegen, The Netherlands; Lale Umutlu, Mark E. Ladd, Stefan Maderwald and Oliver Kraff, Erwin L. Hahn Institute, University Duisburg-Essen, Essen, Germany; Thea Marie Niendorf, Aachen, Germany and Anna Tabea Niendorf, Aachen, Germany who kindly contributed examples of their pioneering work or other valuable assistance. This work was supported (in part, C.O.) by the DZHK (German Centre for Cardiovascular Research) and by the BMBF (Federal Ministry of Education and Research). This work was funded (in part, A.G.) by the Helmholtz Alliance ICEMED – Imaging and Curing Environmental Metabolic Diseases, through the Initiative and Network Fund of the Helmholtz Association (ICEMED-Project 1210251). L.W. and H.W. received support by the BMBF (Federal Ministry of Education and Research, "KMU-innovativ": Medizintechnik MED-373-046).

Figure Captions

Figure 1:

Examples of multi-channel transceiver arrays tailored for cardiac MR at 7.0 T. **Top:** Photographs of cardiac optimized 7.0 T transceiver coil arrays including **(left to right)** a four channel, an eight channel, a 16 channel and a 32 channel loop array configuration together with an eight channel and 16 channel bow tie antenna array. For all configurations the elements are used for transmission and reception. Four chamber (**middle)** and short axis **(bottom)** views of the heart derived from 2D CINE FLASH acquisitions using the RF coil arrays shown on top and a spatial resolution of (1.4 x 1.4. x 4.0) mm^3.

Figure 2:

Examples of multi-channel transceiver arrays tailored for cardiac MR at 7.0 T. **Top:** Photographs of **a)** an eight channel stripline array (61), **b)** an eight channel stripline array which uses automated tuning with piezoelectric actuators (54), **c)** an four channel electric dipole antenna array using fractionated dipoles along with meander structures (66-68), and **d)** an 8 channel dielectric resonant antenna array fabricated with high permittivity, low loss ceramics (55). Four chamber **(middle)** and short axis **(bottom)** views of the heart derived from 2D CINE FLASH acquisitions using the RF coil arrays shown on top. Images courtesy of **a)** Mark E. Ladd, Stefan Maderwald and Oliver Kraff, Erwin L. Hahn Institute, University Duisburg-Essen, Essen, Germany; **b)** Matthew D. Robson, Radcliffe Department of Medicine, University of Oxford, Oxford, UK; **c)** Alexander Raaijmakers, Department of Radiotherapy, University Medical Centre Utrecht, Utrecht, The Netherlands and **d)** Sebastian Aussenhofer, C. J. Gorter Center for High Field Magnetic Resonance, Leiden University Medical Center, Leiden, The Netherlands.

Figure 3:

Example for transmission field assessment with EMF simulations and experimental B_1^+ mapping using a building block equipped with for loop RF elements. For this purpose a cylindrical phantom setup was used in the simulations and in the experiments. **a)** Virtual model of the setup used for validation (RF shield and casing are not shown but included in the simulations). The experimental setup was arranged analogously to the virtual setup. **b)** Simulated B_1^+ distribution (absolute values) of four channels which form one curved building block. For B_1^+ evaluation transversal slices through the cylindrical phantom were positioned in alignment with the center of the loop elements. **c)** Absolute transmission fields derived from B_1^+ mapping of the experimental setup. **d)** Difference maps in percentage of the simulated results. The results demonstrate the qualitative and quantitative agreement between the numerical simulations and the measurements.

Figure 4:

Transmission field shaping using a 32 channel loop element transceiver array (Figure 1d) (53). In this example of static B_1^+ shimming field shaping is based upon EMF simulations for a multi-oblique plane mimicking a four chamber view of the heart. **Top:** B_1^+ field distributions for the three phase setting modes including **left)** an element-wise phase setting approach, **center)** a block-wise optimized phase setting approach were the phase is set identical for four loop elements forming a 4- channel module and **right)** a CP like mode. The element-wise phase setting regime provided the most uniform B_1^+ fields across the heart which is marked by the orange ellipse. The building-block wise RF shimming mode provided a more uniform B_1^+ distribution across the four chamber view of the heart versus the CP-like phase setting regime. **Bottom:** Summary of the phase values used for the three phase setting regimes.

Figure 5:

End-diastolic short axis views covering the heart from the apex to the base derived from 2D CINE FLASH imaging (in-plane resolution (1.1 x 1.1) mm^2, slice thickness 2.5 mm, GRAPPA reduction factor 2,) using **top)** a 32 channel modular TX/RX loop array and **bottom)** a 16 channel modular TX/RX bow tie antenna array. Both array configurations provided rather uniform signal intensity and no major signal voids for slices covering the heart from the apex to the base.

Figure 6:

Four chamber views **(1st row)** and short axis views **(3rd row)** of the heart derived from 2D CINE FLASH acquisitions (GRAPPA reduction factor 2) using **a**,**b)** a 32 channel modular TX/RX loop element array (Figure 1d) and **c**,**d)** a 16 channel modular TX/RX bow tie antenna array (Figure 1f). Different resolution were employed: **a**,**c)** standardized clinical protocol: in-plane resolution=(1.8 x 1.8x6.0) mm^3, **b)** in-plane resolution (1.1 x 1.1x2.5) mm^3 and **d)** in-plane resolution (0.8 x 0.8x2.5) mm^3. **2nd row:** Magnified views of the ventricular trabeculae, demonstrating that spatial resolution enhancements by a factor of six or even twelve versus standardized protocols used in current clinical practice improve the delineation of subtle anatomical details of the heart. **Bottom)** Analysis of the signal intensity in the short axis view using a profile along a circular trajectory inside the myocardium.

Figure 7:

Example for myocardial T_2* mapping at 7.0 T. **Top:** T_2* weighted short axis views of the heart for a mid-ventricular slice derived from multi-echo gradient-echo imaging at 7.0 T. Images shown were obtained with echo times of TE=2.04 ms, TE=4.08 ms, TE=6.12 ms, TE=8.16 ms and TE=10.20 ms. A spatially adaptive non-local means (SANLM) denoising filter was applied (205). **Bottom:** T_2*colour maps of a short axis view of the heart derived from a series of T_2* sensitized 2D CINE acquisitions covering the entire cardiac

cycle (5 cardiac phases out of a series of 21 cardiac phases are shown) overlaid to conventional 2D CINE FLASH images.

Figure 8:

Examples for emerging UHF-CMR applications: **a)** high resolution image of the right coronary artery acquired with a spatial resolution of (0.45 x 0.45 x1.2) mm^3 which was facilitated by a navigator gated free breathing 3D gradient-echo acquisition in conjunction with spectrally selective adiabatic inversion recovery at 7.0 T (courtesy of Maurice M. Bizino and Hildo Lamb, Department of Radiology, Leiden University Medical Center, Leiden, The Netherlands). **b)** fat-water separated (gray scale: water image, colour scale: fat image) coronary artery imaging showing the left main coronary artery using the DIXON approach at 7.0 T. **c)** black blood imaging of a short axis view of the heart derived from high spatial resolution ((0.9 x 0.9 x 4.0) mm^3) fast spin-echo imaging at 7.0 T.

Figure 9:

Examples derived from free breathing real time imaging of a mid-ventricular short axis view of the heart (**left:** systole, **center:** diastole) using an 8 channel bow tie antenna array (Figure 1e) and of the aorta **(right)** using an 16 channel bow tie antenna array (Figure 1f). Images were acquired at a rate of 30 frames per second using highly undersampled radial 2D FLASH with nonlinear inverse reconstruction at a spatial resolution of (1.2 x 1.2 x 6.0) mm^3. The real time images of the aorta demonstrate the 35 cm anatomic coverage of the 16 channel bow tie antenna array along the head-feet direction including details of the liver and the spine without B_1^+ signal voids.

Figure 10:

Examples for renal MRI at 7.0 T. **Top:** TOF-MRA of the renal vasculature. The arrows point at the proximal **(left)** and peripheral **(right)** segments of the renal arteries. The

dashed arrow points at the superior mesenteric artery. The dotted arrows demonstrate the venous overlay, by means of the inferior vena cava and left renal vein. **Bottom:** Non-enhanced **(left)** and post-contrast **(right,** 1-M gadobutrol) T_1-weighted renal VIBE images. (images courtesy of Lale Umutlu, Erwin L. Hahn Institute for Magnetic Resonance Imaging, University Duisburg-Essen, Essen, Germany)

Figure 11:

Examples for liver MRI at 7.0 T. **a)** T_1 weighted image of a central coronal abdominal slice showing a rather uniform excitation across the liver. The image was derived from gradient-echo imaging using a 32 channel TX/RX loop array (Figure 1d) and a voxel size of (0.4x0.4x2.5) mm^3. **b)** Zoomed view of the area marked in red in **a)**. **c)** Zoomed view of a T_1 weighted axial slice covering the liver which was derived from gradient-echo imaging using a 16 channel TX/RX loop array (Figure 1c) and a spatial resolution of (0.3x0.3x2.5) mm^3. No contrast agent was applied. Subtle anatomic liver structures are clearly identifiable including capillaries in the dimension of a diameter of 0.5mm. **d)** Abdominal T_2* map showing a rather uniform T_2* distribution across the liver.

Figure 12:

Axial **(left)**, sagittal **(center)** and coronal **(right)** T_2-weighted images of the prostate of a patient (weight 98 kg, age 58 years, PSA 6 ng/ml) at 7.0 T (courtesy of Tom W. J. Scheenen Department of Radiology, Radboud University Medical Centre, Nijmegen, The Netherlands). For data acquisition a fast spin-echo imaging technique was used: TR=3000 ms, TE=71 ms, FOV=(240 x 180) mm^2, matrix 320 x 240, in-plane spatial resolution=(0.75 x 0.75) mm^2, phase encoding direction: anterior-posterior, slice thickness=3 mm, slice gap=0.6 mm, interleaved slice acquisition, 9 echoes, echo spacing 17.8 ms, readout bandwidth 116 Hz/pixel, NA=1, total acquisition time<2 min. To reduce RF power deposition a prolonged 150^0 RF pulse as used for refocusing. An 8 channel external stripline array was used for TX/RX and B_1+-shimming was applied.

Figure 13:

Top: Sodium images of a four chamber view of the heart **(left)** and a coronal view of the kidneys **(right)** acquired at 7.0 T. The ^{23}Na image of the heart was acquired using a density-adapted 3D radial technique (157) with TE= 0.4 ms, TR=11 ms, TRO= 7.1 ms, TX amplitude 115V (~90% SAR) equivalent to a tip angle of 30-40°, number of projections=50000, number of averages=2 and a voxel size of (6 x 6 x 6) mm³. The ^{23}Na image of the kidneys (courtesy of Stefan Haneder, Institute of Clinical Radiology and Nuclear Medicine, University Medical Center Mannheim, Heidelberg University, Heidelberg, Germany) was acquired with a spatial resolution of (4 x 4 x 5) mm^3 using a 3D Cartesian spoiled gradient-echo sequence with a variable echo time scheme and a highly asymmetric readout (FOV=(256×256) mm^2; matrix size=64×64; number of slices=24; echo time (TE)=4.19 ms; TR=49 ms, total scan time=approximately 40 min). **Bottom:** ^{1}H four chamber view of the heart **(left)** derived from 2D CINE gradient-echo imaging at 7.0 T and ^{1}H coronal view of the kidney obtained at 3.0 T **(right)**.

Figure 14:

Examples for ^{31}P MR spectroscopy **left)** of the heart (courtesy of Christopher Rodgers, Radcliffe Department of Medicine, University of Oxford, Oxford, UK) and **right)** of the prostate (courtesy of Tom W. J. Scheenen Department of Radiology, Radboud University Medical Centre, Nijmegen, The Netherlands). **Left:** Comparison of single voxel ^{31}P spectra of the human heart obtained at 3.0T (blue) and at 7.0 T (red). The voxel used for ^{31}P MRS was placed in the middle of the interventricular septum as illustrated in the short axis view of the heart obtained from a 2D CINE FLASH localizer scan at 7.0 T. ^{31}P MRS at 7.0 T provided an SNR advantage over ^{31}P MR spectroscopy at 3.0 T. **Right:** ^{31}P spectra of a 72-year-old patient with prostate cancer (Gleason score, 4+5; volume, 1.5 cm3) in the peripheral zone on the right side of the gland. The tumor lesion is indicated by white arrows on the transversal T_2-weighted image. The

spectral map shows good quality of ^{31}P spectra across the whole prostate. ^{31}P spectra of the tumor (red circle, red frame) and healthy region (green circle, green frame) are shown separately with the following resonances: phosphoethanolamine (PE), phosphocholine (PC), two phosphate peaks (Pi1 and Pi2), glycerophosphoethanolamine (GPE), glycerophosphocholine (GPC), Phosphocreatine (PCr), gamma-ATP and alpha-ATP. ^{31}P spectra were derived from spectroscopic imaging using a pulse acquire sequence with a 45 degree adiabatic excitation BIR-4 pulse (duration=8 milliseconds), TR=1.5 ms, FOV=(120 x120x120) mm^3; matrix size=10 x10x10, number of averages=12 resulting in voxel volumes of 5.1 cm^3 after apodization with a Hanning filter of the k-space weighted sampling. Total acquisition time was 9 minutes 51 seconds.

Figure 15:

B_1^+ distribution and RF power deposition derived from EMF simulations at 1.5 T, 3.0 T, 7.0 T, 11.7.0 T and 14.0 T using a four channel TX/RX loop array and the torso of the human voxel model "Duke". For each field strength B_1^+ efficiency distribution is scaled to the maximum local SAR. For each configuration identical phase settings are used for B_1^+ and local SAR (10g average, 1W input power) calculations. The $B_1^+/\sqrt{kW}/\sqrt{Max\ local\ SAR_{10g}}$ distribution is shown for 64 MHz 128 MHz, 300 MHz, 500 MHz and 600 MHz and normalized to an efficiency of $30\mu T/\sqrt{kW}\sqrt{W/kg}$. B_1^+ uniformity is substantially reduced for the short wave length regime for $B_0 \geq 7.0$ T. For the maximum input power of the coils, which is dictated by MR safety regulations that forbid overriding of maximum local SAR, a lower B_1^+ field is generated while moving from 1.5 T to 14.0 T. This demonstrates that a higher average power is required for the excitation pulse to reach the same flip angle at higher MR frequencies. Given a higher average power and assuming that TR is not prolonged, RF power deposition shows to be significantly enhanced at UHF-MR frequencies ranging between 300 MHz (7.0 T) and 600 MHz (14.0 T).

Figure 16:

EMF simulations using the human voxel model „Duke" from the virtual family and an 8 channel transmit/receive bow tie electric dipole array. **a)** Schematic views of the positioning of the anterior bow tie RF antennas on the anterior chest of the human voxel model and coronal view of $SAR_{1g\ baseline}$ distribution for a plane through the target position without the stent equivalent being present. **b)** Surface plot of $SAR_{1g\ stent}$ derived from equation 3 for baseline $SAR_{1g\ baseline}$ for an input power of 1W/kg. A stent length ranging from 10-40 mm and a stent rotation versus the main *E*-field vector ranging from $0\text{-}90^0$ was applied. **c)** Coronal view of $SAR_{1g\ stent}$ distribution for a plane through the target position with the stent equivalent being present. **d)** Simulated maximum baseline $SAR_{1g\ baseline}$ and $SAR_{1g\ stent}$ for the stent equivalent using eight randomly generated phase settings compared to the SAR estimation deduced from the analytical approach (equation 3). While conservatively overestimating SAR, SAR estimation using equation 3 was able to predict the induced SAR_{1g} levels without the need to perform extra time consuming EMF simulations with a stent being present in the simulation model.

References

1. van den Bergen B, Van den Berg CAT, Bartels LW, Lagendijk JJW. 7 T body MRI: B1 shimming with simultaneous SAR reduction. Physics in Medicine and Biology 2007;52:5429.

2. Metzger GJ, Snyder C, Akgun C, Vaughan T, Ugurbil K, Van de Moortele PF. Local B1+ shimming for prostate imaging with transceiver arrays at 7T based on subject-dependent transmit phase measurements. Magn Reson Med 2008;59(2):396-409.

3. van den Bergen B, van den Berg CA, Klomp DW, Lagendijk JJ. SAR and power implications of different RF shimming strategies in the pelvis for 7T MRI. J Magn Reson Imaging 2009;30(1):194-202.

4. Umutlu L, Kraff O, Orzada S, Fischer A, Kinner S, Maderwald S, Antoch G, Quick HH, Forsting M, Ladd ME, Lauenstein TC. Dynamic Contrast-Enhanced Renal MRI at 7 Tesla: Preliminary Results. Invest Radiol 2011;46(7):425-433.

5. Umutlu L, Orzada S, Kinner S, Maderwald S, Brote I, Bitz AK, Kraff O, Ladd SC, Antoch G, Ladd ME, Quick HH, Lauenstein TC. Renal imaging at 7 Tesla: preliminary results. Eur Radiol 2011;21(4):841-849.

6. van den Bergen B, Klomp DW, Raaijmakers AJ, de Castro CA, Boer VO, Kroeze H, Luijten PR, Lagendijk JJ, van den Berg CA. Uniform prostate imaging and spectroscopy at 7 T: comparison between a microstrip array and an endorectal coil. NMR Biomed 2011;24(4):358-365.

7. Umutlu L, Maderwald S, Kraff O, Kinner S, Schaefer LC, Wrede K, Antoch G, Forsting M, Ladd ME, Lauenstein TC, Quick HH. New look at renal vasculature: 7 tesla nonenhanced T1-weighted FLASH imaging. J Magn Reson Imaging 2012;36(3):714-721.

8. Snyder CJ, Delabarre L, Moeller S, Tian J, Akgun C, Van de Moortele PF, Bolan PJ, Ugurbil K, Vaughan JT, Metzger GJ. Comparison between eight- and sixteen-channel TEM transceive arrays for body imaging at 7 T. Magn Reson Med 2012;67(4):954-964.

9. Arteaga de Castro CS, van den Bergen B, Luijten PR, van der Heide UA, van Vulpen M, Klomp DW. Improving SNR and B1 transmit field for an endorectal coil in 7 T MRI and MRS of prostate cancer. Magn Reson Med 2012;68(1):311-318.

10. Kobus T, Bitz AK, van Uden MJ, Lagemaat MW, Rothgang E, Orzada S, Heerschap A, Scheenen TW. In vivo 31P MR spectroscopic imaging of the human prostate at 7 T: safety and feasibility. Magn Reson Med 2012;68(6):1683-1695.

11. Umutlu L, Maderwald S, Kinner S, Kraff O, Bitz AK, Orzada S, Johst S, Wrede K, Forsting M, Ladd ME, Lauenstein TC, Quick HH. First-pass contrast-enhanced renal MRA at 7 Tesla: initial results. Eur Radiol 2013;23(4):1059-1066.

12. Metzger GJ, Auerbach EJ, Akgun C, Simonson J, Bi X, Ugurbil K, van de Moortele PF. Dynamically applied B1+ shimming solutions for non-contrast enhanced renal angiography at 7.0 Tesla. Magn Reson Med 2013;69(1):114-126.

13. Luttje MP, Italiaander MG, Arteaga de Castro CS, van der Kemp WJ, Luijten PR, van Vulpen M, van der Heide UA, Klomp DW. 31P MR spectroscopic imaging combined with 1H MR spectroscopic imaging in the human prostate using a double tuned endorectal coil at 7T. Magn Reson Med 2014;72(6):1516-1521.

14. Umutlu L, Kraff O, Fischer A, Kinner S, Maderwald S, Nassenstein K, Nensa F, Gruneisen J, Orzada S, Bitz AK, Forsting M, Ladd ME, Lauenstein TC. Seven-Tesla MRI of the female pelvis. Eur Radiol 2013;23(9):2364-2373.

15. Wu X, Schmitter S, Auerbach EJ, Ugurbil K, Van de Moortele PF. Mitigating transmit B 1 inhomogeneity in the liver at 7T using multi-spoke parallel transmit RF pulse design. Quant Imaging Med Surg 2014;4(1):4-10.

16. Vos EK, Lagemaat MW, Barentsz JO, Futterer JJ, Zamecnik P, Roozen H, Orzada S, Bitz AK, Maas MC, Scheenen TW. Image quality and cancer visibility of T2-weighted magnetic resonance imaging of the prostate at 7 Tesla. Eur Radiol 2014;24(8):1950-1958.

17. Maas MC, Vos EK, Lagemaat MW, Bitz AK, Orzada S, Kobus T, Kraff O, Maderwald S, Ladd ME, Scheenen TW. Feasibility of T2 -weighted turbo spin echo imaging of the human prostate at 7 tesla. Magn Reson Med 2014;71(5):1711-1719.

18. Johst S, Orzada S, Fischer A, Umutlu L, Ladd ME, Maderwald S. Comparison of fat saturation techniques for single-shot fast spin echo sequences for 7-T body imaging. Invest Radiol 2014;49(2):101-108.

19. Fischer A, Kraff O, Orzada S, Nensa F, Schafer LC, Ladd ME, Umutlu L, Lauenstein TC. Ultrahigh-field imaging of the biliary tract at 7 T: initial results of

gadoxetic acid-enhanced magnetic resonance cholangiography. Invest Radiol 2014;49(5):346-353.

20. Haneder S, Juras V, Michaely HJ, Deligianni X, Bieri O, Schoenberg SO, Trattnig S, Zbyn S. In vivo sodium (23Na) imaging of the human kidneys at 7 T: preliminary results. Eur Radiol 2014;24(2):494-501.

21. Fischer A, Kraff O, Maderwald S, Beiderwellen K, Ladd ME, Forsting M, Lauenstein TC, Umutlu L. Non-enhanced T1-weighted liver vessel imaging at 7 Tesla. PLoS One 2014;9(6):e97465.

22. Lagemaat MW, Vos EK, Maas MC, Bitz AK, Orzada S, van Uden MJ, Kobus T, Heerschap A, Scheenen TW. Phosphorus magnetic resonance spectroscopic imaging at 7 T in patients with prostate cancer. Invest Radiol 2014;49(5):363-372.

23. Lagemaat MW, Maas MC, Vos EK, Bitz AK, Orzada S, Weiland E, van Uden MJ, Kobus T, Heerschap A, Scheenen TW. 31P MR spectroscopic imaging of the human prostate at 7 T: T1 relaxation times, Nuclear Overhauser Effect, and spectral characterization. Magn Reson Med 2014; doi: 10.1002/mrm.25209. [Epub ahead of print].

24. Kraff O, Fischer A, Nagel AM, Monninghoff C, Ladd ME. MRI at 7 tesla and above: Demonstrated and potential capabilities. J Magn Reson Imaging 2015;41(1):13-33.

25. Vaughan JT, Snyder CJ, DelaBarre LJ, Bolan PJ, Tian J, Bolinger L, Adriany G, Andersen P, Strupp J, Ugurbil K. Whole-body imaging at 7T: preliminary results. Magn Reson Med 2009;61(1):244-248.

26. Snyder CJ, DelaBarre L, Metzger GJ, van de Moortele PF, Akgun C, Ugurbil K, Vaughan JT. Initial results of cardiac imaging at 7 Tesla. Magn Reson Med 2009;61(3):517-524.

27. Frauenrath T, Hezel F, Heinrichs U, Kozerke S, Utting JF, Kob M, Butenweg C, Boesiger P, Niendorf T. Feasibility of cardiac gating free of interference with electro-magnetic fields at 1.5 Tesla, 3.0 Tesla and 7.0 Tesla using an MR-stethoscope. Invest Radiol 2009;44(9):539-547.

28. Brandts A, Westenberg JJ, Versluis MJ, Kroft LJ, Smith NB, Webb AG, de Roos A. Quantitative assessment of left ventricular function in humans at 7 T. Magn Reson Med 2010;64(5):1471-1477.

29. van Elderen SG, Versluis MJ, Webb AG, Westenberg JJ, Doornbos J, Smith NB, de Roos A, Stuber M. Initial results on in vivo human coronary MR angiography at 7 T. Magn Reson Med 2009;62(6):1379-1384.

30. van Elderen SG, Versluis MJ, Westenberg JJ, Agarwal H, Smith NB, Stuber M, de Roos A, Webb AG. Right coronary MR angiography at 7 T: a direct quantitative and qualitative comparison with 3 T in young healthy volunteers. Radiology 2010;257(1):254-259.

31. Versluis MJ, Tsekos N, Smith NB, Webb AG. Simple RF design for human functional and morphological cardiac imaging at 7tesla. J Magn Reson 2009;200(1):161-166.

32. Niendorf T, Sodickson DK, Krombach GA, Schulz-Menger J. Toward cardiovascular MRI at 7 T: clinical needs, technical solutions and research promises. Eur Radiol 2010;20(12):2806-2816.

33. Frauenrath T, Hezel F, Renz W, d'Orth Tde G, Dieringer M, von Knobelsdorff-Brenkenhoff F, Prothmann M, Schulz Menger J, Niendorf T. Acoustic cardiac triggering: a practical solution for synchronization and gating of cardiovascular magnetic resonance at 7 Tesla. J Cardiovasc Magn Reson 2010;12:67.

34. von Knobelsdorff-Brenkenhoff F, Frauenrath T, Prothmann M, Dieringer MA, Hezel F, Renz W, Kretschel K, Niendorf T, Schulz-Menger J. Cardiac chamber quantification using magnetic resonance imaging at 7 Tesla--a pilot study. Eur Radiol 2010;20(12):2844-2852.

35. Dieringer MA, Renz W, Lindel T, Seifert F, Frauenrath T, von Knobelsdorff-Brenkenhoff F, Waiczies H, Hoffmann W, Rieger J, Pfeiffer H, Ittermann B, Schulz-Menger J, Niendorf T. Design and application of a four-channel transmit/receive surface coil for functional cardiac imaging at 7T. J Magn Reson Imaging 2011;33(3):736-741.

36. Suttie JJ, Delabarre L, Pitcher A, van de Moortele PF, Dass S, Snyder CJ, Francis JM, Metzger GJ, Weale P, Ugurbil K, Neubauer S, Robson M, Vaughan T. 7 Tesla (T) human cardiovascular magnetic resonance imaging using FLASH and SSFP to assess cardiac function: validation against 1.5 T and 3 T. NMR Biomed 2012;25(1):27-34.

37. Grassl A, Winter L, Thalhammer C, Renz W, Kellman P, Martin C, von Knobelsdorff-Brenkenhoff F, Tkachenko V, Schulz-Menger J, Niendorf T. Design,

evaluation and application of an eight channel transmit/receive coil array for cardiac MRI at 7.0 T. Eur J Radiol 2013;82(5):752-759.

38. Winter L, Kellman P, Renz W, Grassl A, Hezel F, Thalhammer C, von Knobelsdorff-Brenkenhoff F, Tkachenko V, Schulz-Menger J, Niendorf T. Comparison of three multichannel transmit/receive radiofrequency coil configurations for anatomic and functional cardiac MRI at 7.0T: implications for clinical imaging. Eur Radiol 2012;22(10):2211-2220.

39. Thalhammer C, Renz W, Winter L, Hezel F, Rieger J, Pfeiffer H, Graessl A, Seifert F, Hoffmann W, von Knobelsdorff-Brenkenhoff F, Tkachenko V, Schulz-Menger J, Kellman P, Niendorf T. Two-dimensional sixteen channel transmit/receive coil array for cardiac MRI at 7.0 T: design, evaluation, and application. J Magn Reson Imaging 2012;36(4):847-857.

40. Frauenrath T, Fuchs K, Dieringer MA, Ozerdem C, Patel N, Renz W, Greiser A, Elgeti T, Niendorf T. Detailing the use of magnetohydrodynamic effects for synchronization of MRI with the cardiac cycle: a feasibility study. J Magn Reson Imaging 2012;36(2):364-372.

41. Santoro D, Winter L, Muller A, Vogt J, Renz W, Ozerdem C, Grassl A, Tkachenko V, Schulz-Menger J, Niendorf T. Detailing radio frequency heating induced by coronary stents: a 7.0 Tesla magnetic resonance study. PLoS One 2012;7(11):e49963.

42. Hezel F, Thalhammer C, Waiczies S, Schulz-Menger J, Niendorf T. High spatial resolution and temporally resolved T2* mapping of normal human myocardium at 7.0 Tesla: an ultrahigh field magnetic resonance feasibility study. PLoS One 2012;7(12):e52324.

43. Niendorf T, Graessl A, Thalhammer C, Dieringer MA, Kraus O, Santoro D, Fuchs K, Hezel F, Waiczies S, Ittermann B, Winter L. Progress and promises of human cardiac magnetic resonance at ultrahigh fields: a physics perspective. J Magn Reson 2013;229:208-222.

44. von Knobelsdorff-Brenkenhoff F, Tkachenko V, Winter L, Rieger J, Thalhammer C, Hezel F, Graessl A, Dieringer MA, Niendorf T, Schulz-Menger J. Assessment of the right ventricle with cardiovascular magnetic resonance at 7 Tesla. J Cardiovasc Magn Reson 2013;15:23.

45. Niendorf T, Schulz-Menger J. [Cardiovascular ultrahigh field magnetic resonance imaging : challenges, technical solutions and opportunities]. Radiologe 2013;53(5):422-428.

46. Winter L, Ozerdem C, Hoffmann W, Santoro D, Muller A, Waiczies H, Seemann R, Graessl A, Wust P, Niendorf T. Design and evaluation of a hybrid radiofrequency applicator for magnetic resonance imaging and rf induced hyperthermia: electromagnetic field simulations up to 14.0 Tesla and proof-of-concept at 7.0 Tesla. PLoS One 2013;8(4):e61661.

47. Rodgers CT, Piechnik SK, Delabarre LJ, Van de Moortele PF, Snyder CJ, Neubauer S, Robson MD, Vaughan JT. Inversion recovery at 7 T in the human myocardium: measurement of T(1), inversion efficiency and B(1) (+). Magn Reson Med 2013;70(4):1038-1046.

48. Meloni A, Hezel F, Positano V, Keilberg P, Pepe A, Lombardi M, Niendorf T. Detailing magnetic field strength dependence and segmental artifact distribution of myocardial effective transverse relaxation rate at 1.5, 3.0, and 7.0 T. Magn Reson Med 2014;71(6):2224-2230.

49. Schmitter S, DelaBarre L, Wu X, Greiser A, Wang D, Auerbach EJ, Vaughan JT, Ugurbil K, Van de Moortele PF. Cardiac imaging at 7 Tesla: Single- and two-spoke radiofrequency pulse design with 16-channel parallel excitation. Magn Reson Med 2013;70(5):1210-1219.

50. Bizino MB, Bonetti C, van der Geest RJ, Versluis MJ, Webb AG, Lamb HJ. High spatial resolution coronary magnetic resonance angiography at 7 T: comparison with low spatial resolution bright blood imaging. Invest Radiol 2014;49(5):326-330.

51. Tao Y, Hess AT, Keith GA, Rodgers CT, Liu A, Francis JM, Neubauer S, Robson MD. Optimized saturation pulse train for human first-pass myocardial perfusion imaging at 7T. Magn Reson Med 2014; doi: 10.1002/mrm.25262. [Epub ahead of print].

52. Rodgers CT, Clarke WT, Snyder C, Vaughan JT, Neubauer S, Robson MD. Human cardiac 31P magnetic resonance spectroscopy at 7 Tesla. Magn Reson Med 2014;72(2):304-315.

53. Graessl A, Renz W, Hezel F, Dieringer MA, Winter L, Oezerdem C, Rieger J, Kellman P, Santoro D, Lindel TD, Frauenrath T, Pfeiffer H, Niendorf T. Modular 32-channel transceiver coil array for cardiac MRI at 7.0T. Magn Reson Med 2014;72(1):276-290.

54. Keith GA, Rodgers CT, Hess AT, Snyder CJ, Vaughan JT, Robson MD. Automated tuning of an eight-channel cardiac tranceive array at 7 Tesla

using piezoelectric actuators. Magn Reson Med 2014; doi: 10.1002/mrm.25356. [Epub ahead of print].

55. Aussenhofer SA, Webb AG. An eight-channel transmit/receive array of TE01 mode high permittivity ceramic resonators for human imaging at 7T. J Magn Reson 2014;243:122-129.

56. Hess AT, Bissell MM, Ntusi NA, Lewis AJ, Tunnicliffe EM, Greiser A, Stalder AF, Francis JM, Myerson SG, Neubauer S, Robson MD. Aortic 4D flow: Quantification of signal-to-noise ratio as a function of field strength and contrast enhancement for 1.5T, 3T, and 7T. Magn Reson Med 2014; doi: 10.1002/mrm.25317. [Epub ahead of print].

57. Winter L, Oberacker E, Özerdem C, Ji Y, von Knobelsdorff-Brenkenhoff F, Weidemann G, Ittermann B, Seifert F, Niendorf T. On the RF Heating of Intracoronary Stents at 7.0 T. Magn Reson Med 2014; doi: 10.1002/mrm.25483 [Epub ahead of print];(accepted for publication).

58. Schmitter S, Wu X, Ugurbil K, Van de Moortele PF. Design of parallel transmission radiofrequency pulses robust against respiration in cardiac MRI at 7 Tesla. Magn Reson Med 2014, doi: 10.1002/mrm.25512. [Epub ahead of print].

59. Klix S, Els A, Paul K, Graessl A, Oezerdem C, Weinberger O, Winter L, Thalhammer C, Huelnhagen T, Rieger J, Mehling H, Schulz Menger J, Niendorf T. On the Subjective Acceptance during Cardiovascular Magnetic Resonance Imaging at 7.0 Tesla. PLoS One 2015; accepted for publication.

60. Adriany G, Ritter J, Vaughan JT, Ugurbil K, Moortele PF. Experimental Verification of Enhanced B1 Shim Performance with a Z-Encoding RF Coil Array at 7 Tesla. In Proceedings of the Joint Annual Meeting of ISMRM-ESMRMB, Stockholm, Sweden 2010:3831.

61. Maderwald S, Orzada S, Schaefer LC, Bitz AK, Brote I, Kraff O, Theysohn JM, Ladd ME, Ladd SC, Quick HH. 7T Human in vivo Cardiac Imaging with an 8-Channel Transmit/Receive Array. In Proceedings of the 17th Annual Meeting of ISMRM 2009:822.

62. Ipek O, Raaijmakers AJ, Klomp DW, Lagendijk JJ, Luijten PR, van den Berg CA. Characterization of transceive surface element designs for 7 tesla magnetic resonance imaging of the prostate: radiative antenna and microstrip. Phys Med Biol 2012;57(2):343-355.

63. Raaijmakers AJ, Ipek O, Klomp DW, Possanzini C, Harvey PR, Lagendijk JJ, van den Berg CA. Design of a radiative surface coil array element at 7 T: the single-side adapted dipole antenna. Magn Reson Med 2011;66(5):1488-1497.

64. Özerdem C, Winter L, Hoffmann W, Waiczies H, Seeman R, Santoro D, Müller A, Ok A, Lindel T, Ittermann B, Niendorf T. Design and Evaluation of a Dipole Antenna TX/RX Element as a Building Block for Combined MR Imaging and RF Hyperthermia at 7.0 T. In Proceedings of the 20th Annual Meeting of ISMRM, Melbourne, Victoria, Australia 2012:2641.

65. Ipek O, Raaijmakers AJ, Lagendijk JJ, Luijten PR, van den Berg CA. Intersubject local SAR variation for 7T prostate MR imaging with an eight-channel single-side adapted dipole antenna array. Magn Reson Med 2014;71(4):1559-1567.

66. Raaijmakers AJE, El Aidi H, Versluis M, Webb AG, Lamb HJ, Luijten PR, van den Berg CAT, Leiner T. Comprehensive coronary artery imaging at 7.0 T: Proof of feasibility. In Proceedings of the Joint Annual Meeting ISMRM-ESMRMB, Milan, Italy 2014:4923.

67. Raaijmakers AJE, Voogt I, Klomp DWJ, Luijten PR, van den Berg CAT. Dipole antenna without ceramic substrate and still low SAR: the fractionated dipole antenna. In Proceedings of the 21th Annual Meeting of ISMRM, Salt Lake City, Utah, USA 2013;2013:4382.

68. Chen G, Cloos M, Sodickson DK, Wiggins GC. A 7T 8 channel transmit-receive dipole array for head imaging: dipole element and coil evaluation. In Proceedings of the Joint Annual Meeting of ISMRM-ESMRMB, Milan, Italy 2014:621.

69. Chen G, Cloos M, Lattanzi R, Sodickson DK, Wiggins GC. Bent Electric Dipoles: A Novel Coil Design Inspired by the Ideal Current Pattern for Central SNR at 7 Tesla. In: Ismrm, editor. Proc Intl Soc Mag Reson Med 22; 2014. p 402.

70. Lakshmanan K, Cloos M, Lattanzi R, Sodickson DK, Novivkov D, Wiggins GC. The Circular Dipole. In Proceedings of the Joint Meeting ISMRM-ESMRMB, Milan, Italy 2014:315.

71. Lee W, Sodickson DK, Wiggins GC. A new UHF Transceiver Antenna Design: Modified Folded Dipole. In Proceedings of the 21th Annual Meeting of ISMRM, Salt Lake City, Utah, USA 2013:4367.

72. Lattanzi R, Sodickson DK. Ideal current patterns yielding optimal signal-to-noise ratio and specific absorption rate in magnetic resonance imaging:

computational methods and physical insights. Magn Reson Med 2012;68(1):286-304.

73. Wiggins GJ, Zhang B, Lattanzi R, Chen GM, Sodickson DK. The Electric Dipole Array: An Attempt to Match the Ideal Current Pattern for Central SNR at 7 Tesla. In Proceedings of the 20th Annual Meeting of ISMRM, Melbourne, Victoria, Australia; 2012. p 541.

74. Akoka S, Franconi F, Seguin F, Le Pape A. Radiofrequency map of an NMR coil by imaging. Magn Reson Imaging 1993;11(3):437-441.

75. Cunningham CH, Pauly JM, Nayak KS. Saturated double-angle method for rapid B1+ mapping. Magn Reson Med 2006;55(6):1326-1333.

76. Insko EK, Bolinger L. Mapping of the radiofrequency field. J Magn Reson A 1993;103:83-85.

77. Stollberger R, Wach P. Imaging of the active B1 field in vivo. Magn Reson Med 1996;35(2):246-251.

78. Klose U. Mapping of the radio frequency magnetic field with a MR snapshot FLASH technique. Med Phys 1992;19(4):1099-1104.

79. Yarnykh VL. Actual flip-angle imaging in the pulsed steady state: a method for rapid three-dimensional mapping of the transmitted radiofrequency field. Magn Reson Med 2007;57(1):192-200.

80. Dowell NG, Tofts PS. Fast, accurate, and precise mapping of the RF field in vivo using the 180 degrees signal null. Magn Reson Med 2007;58(3):622-630.

81. Stanisz GJ, Odrobina EE, Pun J, Escaravage M, Graham SJ, Bronskill MJ, Henkelman RM. T1, T2 relaxation and magnetization transfer in tissue at 3T. Magn Reson Med 2005;54(3):507-512.

82. Nehrke K, Bornert P. DREAM--a novel approach for robust, ultrafast, multislice B(1) mapping. Magn Reson Med 2012;68(5):1517-1526.

83. Linz P, Santoro D, Renz W, Rieger J, Ruehle A, Ruff J, Deimling M, Rakova N, Muller DN, Luft FC, Titze J, Niendorf T. Skin sodium measured with (23) Na MRI at 7.0 T. NMR Biomed 2015;28(1):54-62.

84. Nehrke K, Sprinkart AM, Bornert P. An in vivo comparison of the DREAM sequence with current RF shim technology. MAGMA 2014; [Epub ahead of print].

85. Boernert P, Nehrke K, Wang J. Magnetization Prepared DREAM for Fast Flow-Robust B1+ Mapping. In Proceedings of theJoint Meeting of ISMRM-ESMRMB, Milan, Italy 2014:4383.

86. Morrell GR, Schabel MC. An analysis of the accuracy of magnetic resonance flip angle measurement methods. Phys Med Biol 2010;55(20):6157-6174.

87. Morrell GR. A phase-sensitive method of flip angle mapping. Magn Reson Med 2008;60(4):889-894.

88. Mugler JPI, Miller GW, Altes TA, de Lange EE, Brookeman JR. A Low-Flip-Angle, Phase-Based Method for Accurately Calibrating the Transmitter in Hyperpolarized-Gas MRI. In Proceedings of the 13th Annual Meeting of ISMRM, Miami Beach, USA 2005:789.

89. Santoro D, Rivoire J, Meise F, Terekhov M, Salhi Z, Gast K, Schreiber LM. Three-dimensional mapping of the B1 field using an optimized phase-based method: application to hyperpolarized 3He in lungs. Magn Reson Med 2011;65(4):1166-1172.

90. Santoro D, von Samson-Himmelstjerna F, Carinci F, Hezel F, Dieringer M, Niendorf T. Cardiac Triggered B1+ mapping using Bloch Siegert in the heart at 3T. In Proceedings of the 20th Annual Meeting of ISMRM, Melbourne, Victoria, Australia 2012:3840.

91. Sacolick LI, Wiesinger F, Hancu I, Vogel MW. B1 mapping by Bloch-Siegert shift. Magn Reson Med 2010;63(5):1315-1322.

92. Curtis AT, Gilbert KM, Klassen LM, Gati JS, Menon RS. Slice-by-slice B1+ shimming at 7 T. Magn Reson Med 2012;68(4):1109-1116.

93. Carinci F, Santoro D, von Samson-Himmelstjerna F, Lindel TD, Dieringer MA, Niendorf T. Characterization of phase-based methods used for transmission field uniformity mapping: a magnetic resonance study at 3.0 T and 7.0 T. PLoS One 2013;8(3):e57982.

94. Nehrke K, Versluis MJ, Webb A, Bornert P. Volumetric B1 (+) mapping of the brain at 7T using DREAM. Magn Reson Med 2014;71(1):246-256.

95. Bitz A, Orzada S, Kraff O, Maderwald S, Quick H, Solbach K, Bahr A, Fautz HP, F. S, M. L. Comparison of simulation-based and measurement-based RF shimming for whole-body MRI at 7 Tesla. In Proceedings of the Joint Annual Meeting of ISMRM-ESMRMB, Stockholm, Sweden 2010:4720.

96. Christ A, Kainz W, Hahn EG, Honegger K, Zefferer M, Neufeld E, Rascher W, Janka R, Bautz W, Chen J. The Virtual Family—development of surface-based anatomical models of two adults and two children for dosimetric simulations. Phys Med Biol 2010;55:N23.

97. Orzada S, Maderwald S, Poser BA, Bitz AK, Quick HH, Ladd ME. RF excitation using time interleaved acquisition of modes (TIAMO) to address B1 inhomogeneity in high-field MRI. Magn Reson Med 2010;64(2):327-333.

98. Orzada S, Johst S, Maderwald S, Bitz AK, Solbach K, Ladd ME. Mitigation of B1(+) inhomogeneity on single-channel transmit systems with TIAMO. Magn Reson Med 2013;70(1):290-294.

99. Lindel T, Greiser A, Waxmann P, Dietterle M, Seifert F, Fontius U, Renz W, Dieringer MA, Frauenrath T, Schulz-Menger J, Niendorf T, Ittermann B. Cardiac CINE MRI at 7 T Using a Transmit Array. In Proceedings of the 20th Annual Meeting of ISMRM, Melbourne, Victoria, Australia 2012:1227.

100. Metzger G, Bi X, DelaBarre L, Shah S, Ugurbil K, van de Moortele P-F, Vaughan T, Zuehlsdorff S. Left Coronary Artery Imaging at 7T: Initial Results Using Multiple B1+ Shimming Algorithms and Targets. In Proceedings of the 21st Annual Meeting of ISMRM, Montreal, Quebec, Canada 2011:116.

101. Schmitter S, Schnell S, Ugurbil K, Markl M, van de Moortele PF. 4D Flow imaging in the aorta at 7T: impact of dynamic RF shimming and kt-acceleration. In Proceedings of the Joint Annual Meeting of ISMRM-ESMRMB, Milan, Italy 2014:992.

102. Xiufeng L, Snyder CJ, van de Moortele P-F, Ugurbil K, Metzger GJ. Non-Contrast Enhanced Human Renal Perfusion Imaging Using Arterial Spin Labeling at 7T: Initial Experience. In Proceedings of the 20th Annual Meeting of ISMRM, Melbourne, Victoria, Australia 2012:1310.

103. Setsompop K, Wald LL, Alagappan V, Gagoski BA, Adalsteinsson E. Magnitude least squares optimization for parallel radio frequency excitation design demonstrated at 7 Tesla with eight channels. Magn Reson in Med 2008;59(4):908–915.

104. Katscher U, Bornert P. Parallel RF transmission in MRI. NMR Biomed 2006;19(3):393-400.

105. Katscher U, Bornert P, Leussler C, van den Brink JS. Transmit SENSE. Magn Reson Med 2003;49(1):144-150.

106. Zhu Y. Parallel excitation with an array of transmit coils. Magn Reson Med 2004;51(4):775-784.

107. Ullmann P, Junge S, Wick M, Seifert F, Ruhm W, Hennig J. Experimental analysis of parallel excitation using dedicated coil setups and simultaneous RF transmission on multiple channels. Magn Reson Med 2005;54(4):994-1001.

108. Sharma A, Bammer R, Stenger VA, Grissom WA. Low peak power multiband spokes pulses for B inhomogeneity-compensated simultaneous multislice excitation in high field MRI. Magn Reson Med 2014; doi: 10.1002/mrm.25455. [Epub ahead of print].

109. Norris DG, Boyacioglu R, Schulz J, Barth M, Koopmans PJ. Application of PINS radiofrequency pulses to reduce power deposition in RARE/turbo spin echo imaging of the human head. Magn Reson Med 2014;71(1):44-49.

110. Kramer CM, Barkhausen J, Flamm SD, Kim RJ, Nagel E. Standardized cardiovascular magnetic resonance imaging (CMR) protocols, society for cardiovascular magnetic resonance: board of trustees task force on standardized protocols. J Cardiovasc Magn Reson 2008;10:35.

111. Kramer CM, Barkhausen J, Flamm SD, Kim RJ, Nagel E. Standardized cardiovascular magnetic resonance (CMR) protocols 2013 update. J Cardiovasc Magn Reson 2013;15:91.

112. Wagenhaus B, Pohlmann A, Dieringer MA, Els A, Waiczies H, Waiczies S, Schulz-Menger J, Niendorf T. Functional and morphological cardiac magnetic resonance imaging of mice using a cryogenic quadrature radiofrequency coil. PLoS One 2012;7(8):e42383.

113. Vitanis V, Manka R, Giese D, Pedersen H, Plein S, Boesiger P, Kozerke S. High resolution three-dimensional cardiac perfusion imaging using compartment-based k-t principal component analysis. Magn Reson Med 2011;65(2):575-587.

114. Schar M, Vonken EJ, Stuber M. Simultaneous B(0)- and B(1)+-map acquisition for fast localized shim, frequency, and RF power determination in the heart at 3 T. Magn Reson Med 2010;63(2):419-426.

115. Reeder SB, Faranesh AZ, Boxermann JL, McVeigh ER. In vivo measurement of T_2^* and field inhomogeneity maps in the human heart at 1.5 T. Magn Reson Med 1998;39:988-998.

116. O'Regan D, Callaghan M, Fitzpatrick J, Naoumova R, Hajnal J, Schmitz S. Cardiac T2* and lipid measurement at 3.0 T-initial experience. Eur Radiol 2008;18:800 - 805.

117. Pepe A, Positano V, Santarelli MF, Sorrentino F, Cracolici E, De Marchi D, Maggio A, Midiri M, Landini L, Lombardi M. Multislice multiecho T2* cardiovascular magnetic resonance for detection of the heterogeneous distribution of myocardial iron overload. J Magn Reson Imaging 2006;23(5):662-668.

118. Dharmakumar R, Arumana JM, Tang R, Harris K, Zhang Z, Li D. Assessment of regional myocardial oxygenation changes in the presence of coronary artery stenosis with balanced SSFP imaging at 3.0 T: theory and experimental evaluation in canines. J Magn Reson Imaging 2008;27(5):1037-1045.

119. Duyn JH, van Gelderen P, Li TQ, de Zwart JA, Koretsky AP, Fukunaga M. High-field MRI of brain cortical substructure based on signal phase. Proc Natl Acad Sci U S A 2007;104(28):11796-11801.

120. Lee J, van Gelderen P, Kuo LW, Merkle H, Silva AC, Duyn JH. T2*-based fiber orientation mapping. Neuroimage 2011;57(1):225-234.

121. Deistung A, Schafer A, Schweser F, Biedermann U, Turner R, Reichenbach JR. Toward in vivo histology: a comparison of quantitative susceptibility mapping (QSM) with magnitude-, phase-, and R2*-imaging at ultra-high magnetic field strength. Neuroimage 2013;65:299-314.

122. Ogawa S, Menon RS, Tank DW, Kim SG, Merkle H, Ellermann JM, Ugurbil K. Functional brain mapping by blood oxygenation level-dependent contrast magnetic resonance imaging. A comparison of signal characteristics with a biophysical model. Biophys J 1993;64(3):803-812.

123. Ziener CH, Kampf T, Reents G, Schlemmer HP, Bauer WR. Spin dephasing in a magnetic dipole field. Phys Rev E Stat Nonlin Soft Matter Phys 2012;85(5 Pt 1):051908.

124. Ziener CH, Kampf T, Melkus G, Jakob PM, Schlemmer HP, Bauer WR. Signal evolution in the local magnetic field of a capillary -- analogy to the damped driven harmonic oscillator. Magn Reson Imaging 2012;30(4):540-553.

125. Hernando D, Vigen KK, Shimakawa A, Reeder SB. R(2) mapping in the presence of macroscopic B(0) field variations. Magn Reson Med 2011;68(3):830-840.

126. Pohlmann A, Arakelyan K, Hentschel J, Cantow K, Flemming B, Ladwig M, Waiczies S, Seeliger E, Niendorf T. Detailing the Relation Between Renal T2* and Renal Tissue pO2 Using an Integrated Approach of Parametric Magnetic

Resonance Imaging and Invasive Physiological Measurements. Invest Radiol 2014;49(8):547-560.

127. Pohlmann A, Hentschel J, Fechner M, Hoff U, Bubalo G, Arakelyan K, Cantow K, Seeliger E, Flemming B, Waiczies H, Waiczies S, Schunck WH, Dragun D, Niendorf T. High temporal resolution parametric MRI monitoring of the initial ischemia/reperfusion phase in experimental acute kidney injury. PLoS One 2013;8(2):e57411.

128. Messroghli DR, Radjenovic A, Kozerke S, Higgins DM, Sivananthan MU, Ridgway JP. Modified Look-Locker inversion recovery (MOLLI) for high-resolution T1 mapping of the heart. Magnetic resonance in medicine : official journal of the Society of Magnetic Resonance in Medicine / Society of Magnetic Resonance in Medicine 2004;52(1):141-146.

129. von Knobelsdorff-Brenkenhoff F, Prothmann M, Dieringer MA, Wassmuth R, Greiser A, Schwenke C, Niendorf T, Schulz-Menger J. Myocardial T1 and T2 mapping at 3 T: reference values, influencing factors and implications. J Cardiovasc Magn Reson 2013;15(1):53.

130. Messroghli DR, Niendorf T, Schulz-Menger J, Dietz R, Friedrich MG. T1 mapping in patients with acute myocardial infarction. J Cardiovasc Magn Reson 2003;5(2):353-359.

131. Piechnik SK, Ferreira VM, Dall'Armellina E, Cochlin LE, Greiser A, Neubauer S, Robson MD. Shortened Modified Look-Locker Inversion recovery (ShMOLLI) for clinical myocardial T1-mapping at 1.5 and 3 T within a 9 heartbeat breathhold. J Cardiovasc Magn Reson 2010;12:69.

132. Dieringer MA, Deimling M, Santoro D, Wuerfel J, Madai VI, Sobesky J, von Knobelsdorff-Brenkenhoff F, Schulz-Menger J, Niendorf T. Rapid parametric mapping of the longitudinal relaxation time t1 using two-dimensional variable flip angle magnetic resonance imaging at 1.5 tesla, 3 tesla, and 7 tesla. PLoS One 2014;9(3):e91318.

133. Hernando D, Kellman P, Haldar JP, Liang ZP. Robust water/fat separation in the presence of large field inhomogeneities using a graph cut algorithm. Magn Reson Med 2010;63(1):79-90.

134. Kellman P, Hezel F, Shah S, Renz W, Thalhammer C, Schulz Menger J, Niendorf T. Fat-water separated imaging at 7T: initial results for cardiac applications. In Proceedings of the 19th Annual Meeting of ISMRM, Montreal, Quebec, Canada 2011:597.

135. Hezel F, Kellman P, Thalhammer C, Özerdem C, Renz W, Niendorf T. Initial Results of Abdominal MRI at 7T Using a 16 channel Transmit/Receive Coil. In Proceedings of the 19th Annual Meeting of ISMRM, Montreal, Quebec, Canada 2011:595.

136. Hezel F, Graessl A, Kellman P, Niendorf T. Feasibility of Abdominal MRI at 7.0 T Using a Novel 32 Channel Transceiver Coil Array. In Proceedings of the 20th Annual Meeting of ISMRM, Melbourne, Victoria, Australia 2012:2808.

137. Niendorf T, Hardy CJ, Giaquinto RO, Gross P, Cline HE, Zhu Y, Kenwood G, Cohen S, Grant AK, Joshi S, Rofsky NM, Sodickson DK. Toward single breath-hold whole-heart coverage coronary MRA using highly accelerated parallel imaging with a 32-channel MR system. Magn Reson Med 2006;56(1):167-176.

138. Niendorf T, Saranathan M, Lingamneni A, Pedrosa I, Spencer M, Cline H, Foo TK, Rofsky NM. Short breath-hold, volumetric coronary MR angiography employing steady-state free precession in conjunction with parallel imaging. Magn Reson Med 2005;53(4):885-894.

139. Hagberg GE, Scheffler K. Effect of r(1) and r(2) relaxivity of gadolinium-based contrast agents on the T(1)-weighted MR signal at increasing magnetic field strengths. Contrast Media Mol Imaging 2013;8(6):456-465.

140. Kalavagunta C, Michaeli S, Metzger GJ. In vitro Gd-DTPA relaxometry studies in oxygenated venous human blood and aqueous solution at 3 and 7 T. Contrast Media Mol Imaging 2014;9(2):169-176.

141. Fuchs K, Hezel F, Klix S, Mekle R, Wuerfel J, Niendorf T. Simultaneous dual contrast weighting using double echo rapid acquisition with relaxation enhancement (RARE) imaging, doi 10.1002/mrm.25066. Magn Reson Med 2014;72(6):1590.

142. Klix S, Hezel F, Fuchs K, Ruff J, Dieringer MA, Niendorf T. Accelerated Fast Spin-Echo Magnetic Resonance Imaging of the Heart Using a Self-Calibrated Split-Echo Approach. PLoS One 2014;9(4):e94654.

143. Voit D, Zhang S, Unterberg-Buchwald C, Sohns JM, Lotz J, Frahm J. Real-time cardiovascular magnetic resonance at 1.5 T using balanced SSFP and 40 ms resolution. J Cardiovasc Magn Reson 2013;15:79.

144. Kowallick JT, Joseph AA, Unterberg-Buchwald C, Fasshauer M, van Wijk K, Merboldt KD, Voit D, Frahm J, Lotz J, Sohns JM. Real-time phase-contrast flow MRI of the ascending aorta and superior vena cava as a function of

intrathoracic pressure (Valsalva manoeuvre). Br J Radiol 2014;87(1042):20140401.

145. Fasshauer M, Joseph AA, Kowallick JT, Unterberg-Buchwald C, Merboldt KD, Voit D, Steinmetz M, Staab W, Schaetz S, Zhang S, Frahm J, Lotz J, Sohns JM. Real-time phase-contrast flow MRI of haemodynamic changes in the ascending aorta and superior vena cava during Mueller manoeuvre. Clin Radiol 2014;69(10):1066-1071.

146. Joseph A, Kowallick JT, Merboldt KD, Voit D, Schaetz S, Zhang S, Sohns JM, Lotz J, Frahm J. Real-time flow MRI of the aorta at a resolution of 40 msec. J Magn Reson Imaging 2014;40(1):206-213.

147. Courtier J, Ohliger M, Rhee SJ, Terreblanche O, Heyman MB, MacKenzie JD. Shooting a moving target: use of real-time cine magnetic resonance imaging in assessment of the small bowel. J Pediatr Gastroenterol Nutr 2013;57(4):426-431.

148. Talasz H, Kremser C, Kofler M, Kalchschmid E, Lechleitner M, Rudisch A. Proof of concept: differential effects of Valsalva and straining maneuvers on the pelvic floor. Eur J Obstet Gynecol Reprod Biol 2012;164(2):227-233.

149. Arakelyan K, Cantow K, Hentschel J, Flemming B, Pohlmann A, Ladwig M, Niendorf T, Seeliger E. Early effects of an x-ray contrast medium on renal T(2)*/T(2) MRI as compared to short-term hyperoxia, hypoxia and aortic occlusion in rats. Acta Physiol (Oxf) 2013;208(2):202-213.

150. Niendorf T, Pohlmann A, Arakelyan K, Flemming B, Cantow K, Hentschel J, Grosenick D, Ladwig M, Reimann H, Klix S, Waiczies S, Seeliger E. How bold is blood oxygenation level-dependent (BOLD) magnetic resonance imaging of the kidney? Opportunities, challenges and future directions. Acta Physiol (Oxf) 2015;213(1):19-38.

151. Cornud F, Delongchamps NB, Mozer P, Beuvon F, Schull A, Muradyan N, Peyromaure M. Value of multiparametric MRI in the work-up of prostate cancer. Curr Urol Rep 2012;13(1):82-92.

152. Akin O, Sala E, Moskowitz CS, Kuroiwa K, Ishill NM, Pucar D, Scardino PT, Hricak H. Transition zone prostate cancers: features, detection, localization, and staging at endorectal MR imaging. Radiology 2006;239(3):784-792.

153. Sala E, Eberhardt SC, Akin O, Moskowitz CS, Onyebuchi CN, Kuroiwa K, Ishill N, Zelefsky MJ, Eastham JA, Hricak H. Endorectal MR imaging before salvage prostatectomy: tumor localization and staging. Radiology 2006;238(1):176-183.

154. Roethke M, Anastasiadis AG, Lichy M, Werner M, Wagner P, Kruck S, Claussen CD, Stenzl A, Schlemmer HP, Schilling D. MRI-guided prostate biopsy detects clinically significant cancer: analysis of a cohort of 100 patients after previous negative TRUS biopsy. World J Urol 2012;30(2):213-218.

155. Madelin G, Regatte RR. Biomedical applications of sodium MRI in vivo. JOURNAL OF MAGNETIC RESONANCE IMAGING 2013;38(3):511–529.

156. Sandstede JJW, Hillenbrand H, Beer M, Pabst T, Butter F, Machann W, Bauer W, Hahn D, Neubauer S. Time course of 23Na signal intensity after myocardial infarction in humans. Magnetic resonance in medicine : official journal of the Society of Magnetic Resonance in Medicine / Society of Magnetic Resonance in Medicine 2004;52(3):545–551.

157. Nagel AM, Laun FB, Weber MA, Matthies C, Semmler W, Schad LR. Sodium MRI using a density-adapted 3D radial acquisition technique. Magn Reson Med 2009;62(6):1565-1573.

158. Resetar A, Hoffmann SH, Graessl A, Waiczies H, Niendorf T, Nagel A. Retrospectively Gated CINE 23Na Imaging of the Heart at 7.0 T Using Density-Adapted 3D Projection Reconstruction. In Proceedings of the Joint Meeting of ISMRM-ESMRMB, Milan, Italy 2014:436.

159. Kopp C, Linz P, Wachsmuth L, Dahlmann A, Horbach T, Schofl C, Renz W, Santoro D, Niendorf T, Muller DN, Neininger M, Cavallaro A, Eckardt KU, Schmieder RE, Luft FC, Uder M, Titze J. (23)Na magnetic resonance imaging of tissue sodium. Hypertension 2012;59(1):167-172.

160. Gnahm C, Bock M, Bachert P, Semmler W, Behl NG, Nagel AM. Iterative 3D projection reconstruction of (23) Na data with an (1) H MRI constraint. Magn Reson Med 2014;71(5):1720-1732.

161. Frauenrath, Tobias, Niendorf, Thoralf, Kob, Malte. Acoustic Method for Synchronization of Magnetic Resonance Imaging (MRI). Acta Acustica united with Acustica 2008;94(1):148-155.

162. Becker M, Frauenrath T, Hezel F, Krombach GA, Kremer U, Koppers B, Butenweg C, Goemmel A, Utting JF, Schulz-Menger J, Niendorf T. Comparison of left ventricular function assessment using phonocardiogram- and electrocardiogram-triggered 2D SSFP CINE MR imaging at 1.5 T and 3.0 T. Eur Radiol 2010;20(6):1344-1355.

163. IEC. 60601-2-33 Medical electrical equipment - Part 2-33: Particular requirements for the basic safety and essential performance of magnetic resonance equipment for medical diagnosis. Edition 3.0. 2010.

164. Wang Z, Lin JC, Mao W, Liu W, Smith MB, Collins CM. SAR and temperature: simulations and comparison to regulatory limits for MRI. Journal of Magnetic Resonance Imaging 2007;26(2):437-441.

165. Murbach M, Neufeld E, Capstick M, Kainz W, Brunner DO, Samaras T, Pruessmann KP, Kuster N. Thermal tissue damage model analyzed for different whole-body SAR and scan durations for standard MR body coils. Magn Reson Med 2014;71(1):421-431.

166. Hoult DI. Sensitivity and Power Deposition in a High-Field Imaging Experiment. Journal of Magnetic Resonance Imaging 2000;12(1):46-67.

167. Collins CM, Smith MB. Calculations of B1 distribution, SNR, and SAR for a surface coil adjacent to an anatomically-accurate human body model. Magnetic Resonance in Medicine 2001;45(4):692-699.

168. Seifert F, Wubbeler G, Junge S, Ittermann B, Rinneberg H. Patient safety concept for multichannel transmit coils. J Magn Reson Imaging 2007;26(5):1315-1321.

169. Lattanzi R, Sodickson D, Grant A, Zhu Y. Electrodynamic constraints on homogeneity and radiofrequency power deposition in multiple coil excitations. Magnetic Resonance in Medicine 2009;61(2):315-334.

170. Zhu Y, Alon L, Deniz CM, Brown R, Sodickson DK. System and SAR characterization in parallel RF transmission. Magn Reson Med 2011;67(5):1367-1378.

171. Graesslin I, Vernickel P, Bornert P, Nehrke K, Mens G, Harvey P, Katscher U. Comprehensive RF safety concept for parallel transmission MR. Magn Reson Med 2014; doi: 10.1002/mrm.25425. [Epub ahead of print].

172. Wolf S, Diehl D, Gebhardt M, Mallow J, Speck O. SAR simulations for high-field MRI: How much detail, effort, and accuracy is needed? Magn Reson Med 2012;69(4):1157-1168.

173. Eichfelder G, Gebhardt M. Local specific absorption rate control for parallel transmission by virtual observation points. Magn Reson Med 2011;66(5):1468-1476.

174. Graesslin I, Homann H, Biederer S, Bornert P, Nehrke K, Vernickel P, Mens G, Harvey P, Katscher U. A specific absorption rate prediction concept for parallel transmission MR. Magn Reson Med 2012;68(5):1664-1674.

175. Homann H, Graesslin I, Eggers H, Nehrke K, Vernickel P, Katscher U, Dossel O, Bornert P. Local SAR management by RF Shimming: a simulation study with multiple human body models. MAGMA 2012;25(3):193-204.

176. Homann H, Bornert P, Eggers H, Nehrke K, Dossel O, Graesslin I. Toward individualized SAR models and in vivo validation. Magn Reson Med 2011;66(6):1767-1776.

177. Voigt T, Homann H, Katscher U, Doessel O. Patient-individual local SAR determination: In vivo measurements and numerical validation. Magn Reson Med 2012;68(4):1117-1126.

178. Murbach M, Neufeld E, Pruessmann KP, Kuster N. Safe MR scan times based on CEM43 tissue damage thresholds, using electromagnetic and thermal simulations with anatomically correct human models and considering local thermoregulation. In Proceedings of the 20th Annual Meeting of ISMRM, Melbourne, Victoria, Australia 2012:313.

179. Yarmolenko PS, Moon EJ, Landon C, Manzoor A, Hochman DW, Viglianti BL, Dewhirst MW. Thresholds for thermal damage to normal tissues: An update. International Journal of Hyperthermia 2011;27(4):320-343.

180. Oh S, Webb AG, Neuberger T, Park B, Collins CM. Experimental and numerical assessment of MRI-induced temperature change and SAR distributions in phantoms and in vivo. Magn Reson Med 2010;63(1):218-223.

181. Oh S, Ryu YC, Carluccio G, Sica CT, Collins CM. Measurement of SAR-induced temperature increase in a phantom and in vivo with comparison to numerical simulation. Magn Reson Med 2014;71(5):1923-1931.

182. Eryaman Y, Akin B, Atalar E. Reduction of implant RF heating through modification of transmit coil electric field. Magn Reson Med 2011;65(5):1305-1313.

183. Etezadi-Amoli M, Stang P, Kerr A, Pauly J, Scott G. Controlling radiofrequency-induced currents in guidewires using parallel transmit. Magn Reson Med 2014; DOI 10.1002/mrm.25543 [epub ahead of print].

184. Langereis S, Keupp J, van Velthoven JL, de Roos IH, Burdinski D, Pikkemaat JA, Grull H. A temperature-sensitive liposomal 1H CEST and 19F contrast agent for MR image-guided drug delivery. J Am Chem Soc 2009;131(4):1380-1381.

185. Virtanen H, Huttunen J, Toropainen A, Lappalainen R. Interaction of mobile phones with superficial passive metallic implants. Phys Med Biol 2005;50(11):2689.

186. Bakhai A, Booth J, Delahunty N, Nugara F, Clayton T, McNeill J, Davies S, Cumberland D, Stables R. The SV stent study: a prospective, multicentre, angiographic evaluation of the BiodivYsio phosphorylcholine coated small vessel stent in small coronary vessels. Int J Cardiol 2005;102(1):95-102.

187. Ansems J, Kolk A, Kroeze H, Van den Berg NAT, Borst G, Luijten PR, Webb AG, Renema WKJ, Klomp DWJ. MR Imaging of Patients with Stents is Safe at 7.0 Tesla. Proc Intl Soc Mag Reson Med 2012:2764.

188. Oberacker E, Winter L, Seifert F, Marek J, Weidemann G, Hoffmann E, Niendorf T. En Route to Ultrahigh Field Cardiac MR in Patients: RF Safety Assessment of Intracoronary Stents at 7.0T Using Numerical Simulations and E-Field Measurements. In Proceedings of the Joint Meeting of ISMRM-ESMRB, Milan, Italy 2014:0177.

189. Eichfelder G, Gebhardt M. Local specific absorption rate control for parallel transmission by virtual observation points. Magn Reson Med 2011;66(5):1468-1476.

190. Graessl A, Muhle M, Schwerter M, Rieger J, Oezerdem C, Santoro D, Lysiak D, Winter L, Hezel F, Waiczies S, Guthoff RF, Falke K, Hosten N, Hadlich S, Krueger PC, Langner S, Stachs O, Niendorf T. Ophthalmic magnetic resonance imaging at 7 T using a 6-channel transceiver radiofrequency coil array in healthy subjects and patients with intraocular masses. Invest Radiol 2014;49(5):260-270.

191. Lindner T, Langner S, Graessl A, Rieger J, Schwerter M, Muhle M, Lysiak D, Kraus O, Wuerfel J, Guthoff RF, Falke K, Hadlich S, Krueger PC, Hosten N, Niendorf T, Stachs O. High spatial resolution in vivo magnetic resonance imaging of the human eye, orbit, nervus opticus and optic nerve sheath at 7.0 Tesla. Exp Eye Res 2014;125:89-94.

192. Walter U, Niendorf T, Graessl A, Rieger J, Kruger PC, Langner S, Guthoff RF, Stachs O. Ultrahigh field magnetic resonance and colour Doppler real-time fusion imaging of the orbit--a hybrid tool for assessment of choroidal melanoma. Eur Radiol 2014;24(5):1112-1117.

193. Paul K, Graessl A, Rieger R, Lysiak D, Huelnhagen T, Winter L, Heidemann R, Lindner T, Hadlich S, Zimpfer A, Pohlmann A, Endemann B, Krüger PC, Langner

S, Stachs O, Niendorf T. Diffusion-Sensitized Ophthalmic MRI Free of Geometric Distortion at 3.0 T and 7.0 T: A Feasibility Study in Healthy Subjects and Patients with Intraocular Masses. Invest Radiol 2015; accepted for publication.

194. Poulo L, Alon L, Deniz C, Haefner R, Sodickson D, Stoeckel B, Zhu Y. A 32-Channel Parallel Exciter/Amplifier Transmit System for 7T Imaging. In: ISMRM, editor. Proc Intl Soc Mag Reson Med 19; 2011. p 1867.

195. Gudino N, Heilman JA, Riffe MJ, Heid O, Vester M, Griswold MA. On-coil multiple channel transmit system based on class-D amplification and pre-amplification with current amplitude feedback. Magn Reson Med 2013;70(1):276-289.

196. Linz P, Santoro D, Renz W, Ruff J, Deimling M, Muller DN, Titze J, Luft FC, Niendorf T. Age dependent Changes of Sodium Content in Human Calf Skin measured with Sub-Millimeter Spatial Resolution 23Na MRI at 7.0 T. In Proceedings of the 20th Annual Meeting of ISMRM, Melbourne, Victoria, Australia 2012:4372.

197. Umathum R, Rosler MB, Nagel AM. In vivo 39K MR imaging of human muscle and brain. Radiology 2013;269(2):569-576.

198. Nagel AM, Lehmann-Horn F, Weber MA, Jurkat-Rott K, Wolf MB, Radbruch A, Umathum R, Semmler W. In Vivo Cl MR Imaging in Humans: A Feasibility Study. Radiology 2014:131725.

199. Linz P, Santoro D, Renz W, Rieger J, Ruehle A, Ruff J, Deimling M, Rakova N, Mueller DM, Titze J, Luft FC, Niendorf T. Skin Sodium Measured with 23Na Magnetic Resonance Imaging at 7.0 Tesla. NMR Biomed 2015;28(1):54-62.

200. Hoffmann SH, Radbruch A, Bock M, Semmler W, Nagel AM. Direct 17O MRI with partial volume correction: first experiences in a glioblastoma patient. MAGMA 2014;27(6):579-587.

201. Tian J, Shrivastava D, Strupp J, Zhang J, Vaughan JT. From 7T to 10.5T: B1+, SAR and Temperature Distribution for Head and Body MRI. In Proceedings of the 20th Annual Meeting of ISMRM, Melbourne, Victoria, Australia 2012:2666.

202. Committee to Assess the Current Status and Future Direction of High Magnetic Field Science in the United States; Board on Physics and Astronomy; Division on Engineering and Physical Sciences; National Research Council. Washington, DC, USA: The National Academies Press 2013. 232 p.

203. Fu R, Brey WW, Shetty K, Gor'kov P, Saha S, Long JR, Grant SC, Chekmenev EY, Hu J, Gan Z, Sharma M, Zhang F, Logan TM, Bruschweller R, Edison A, Blue A,

Dixon IR, Markiewicz WD, Cross TA. Ultra-wide bore 900 MHz high-resolution NMR at the National High Magnetic Field Laboratory. J Magn Reson 2005;177(1):1-8.

204. Smeibidl P, Bird MD, Ehmler H, Tennant A. New hybrid magnet system for structure research at highest magnetic fields and temperatures in the millikelvin region. Journal of Physics: Conference Series 2012;400:052034.

205. Manjon JV, Coupe P, Marti-Bonmati L, Collins DL, Robles M. Adaptive non-local means denoising of MR images with spatially varying noise levels. J Magn Reson Imaging 2010;31(1):192-203.

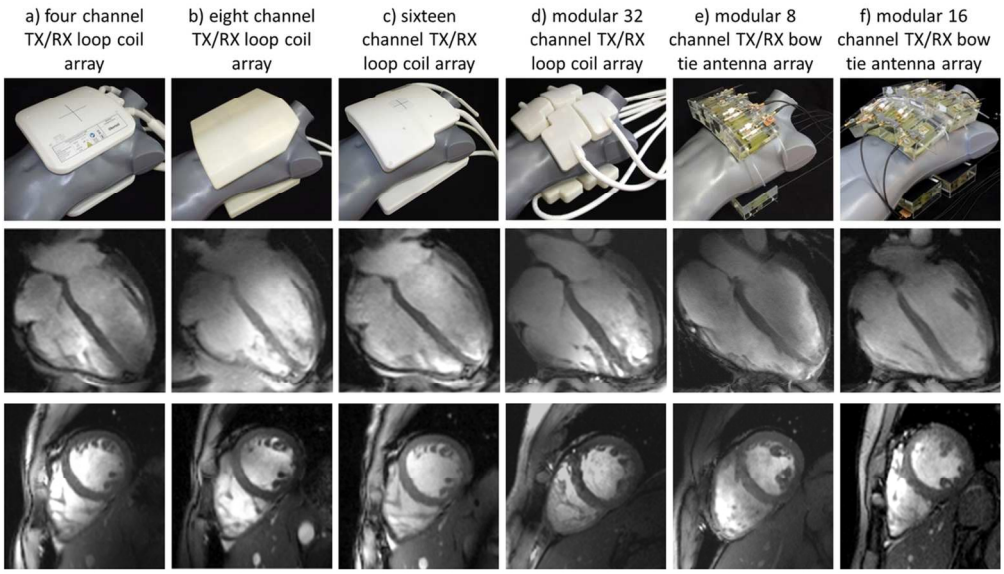

Figure 1:
Examples of multi-channel transceiver arrays tailored for cardiac MR at 7.0 T. Top: Photographs of cardiac optimized 7.0 T transceiver coil arrays including (left to right) a four-channel, an eight channel, a 16 channel and a 32 channel loop array configuration together with an eight channel and 16 channel bow tie antenna array. For all configurations the elements are used for transmission and reception. Four chamber (middle) and short axis (bottom) views of the heart derived from 2D CINE FLASH acquisitions using the RF coil arrays shown on top and a spatial resolution of (1.4 x 1.4. x 4.0) mm^3.

113x64mm (300 x 300 DPI)

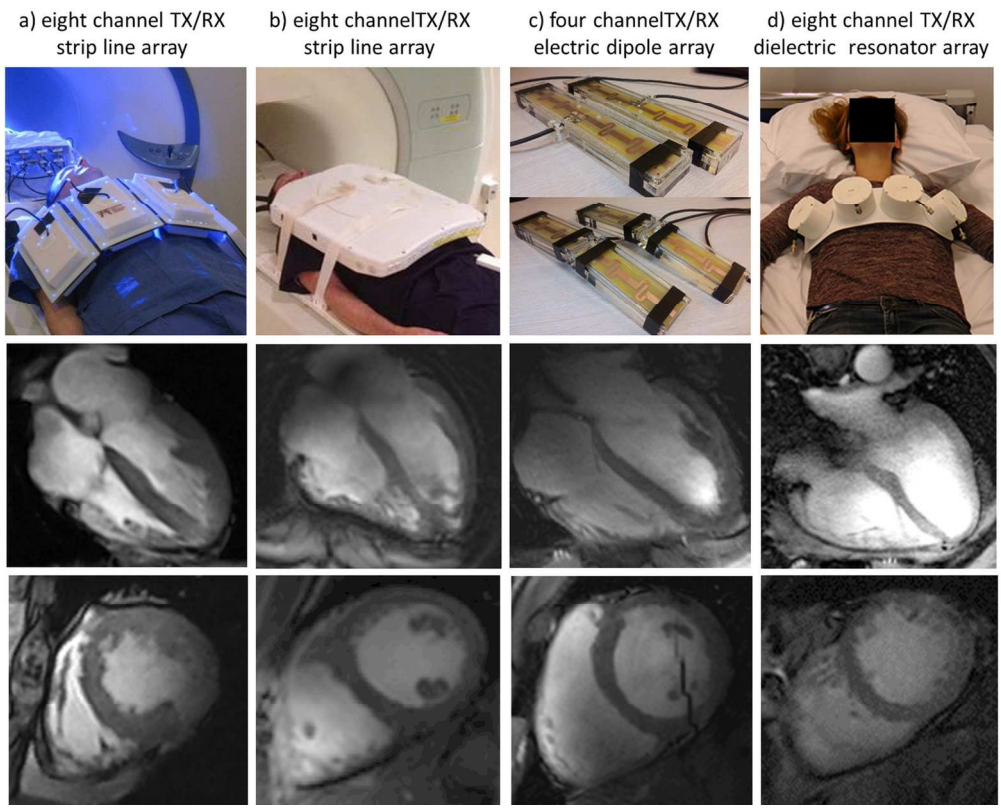

Figure 2:
Examples of multi-channel transceiver arrays tailored for cardiac MR at 7.0 T. Top: Photographs of a) an eight channel stripline array (59), b) an eight channel stripline array which uses automated tuning with piezoelectric actuators (54), c) an four-channel electric dipole antenna array using fractionated dipoles along with meander structures (64-66), and d) an 8 channel dielectric resonant antenna array fabricated with high permittivity, low loss ceramics (55). Four chamber (middle) and short axis (bottom) views of the heart derived from 2D CINE FLASH acquisitions using the RF coil arrays shown on top. Images courtesy of a) Mark E. Ladd, Stefan Maderwald and Oliver Kraff, Erwin L. Hahn Institute, University Duisburg-Essen, Essen, Germany; b) Matthew D. Robson, Radcliffe Department of Medicine, University of Oxford, Oxford, UK; c) Alexander Raaijmakers, Department of Radiotherapy, University Medical Centre Utrecht, Utrecht, The Netherlands and d) Sebastian Aussenhofer, C. J. Gorter Center for High Field Magnetic Resonance, Leiden University Medical Center, Leiden, The Netherlands.
159x127mm (300 x 300 DPI)

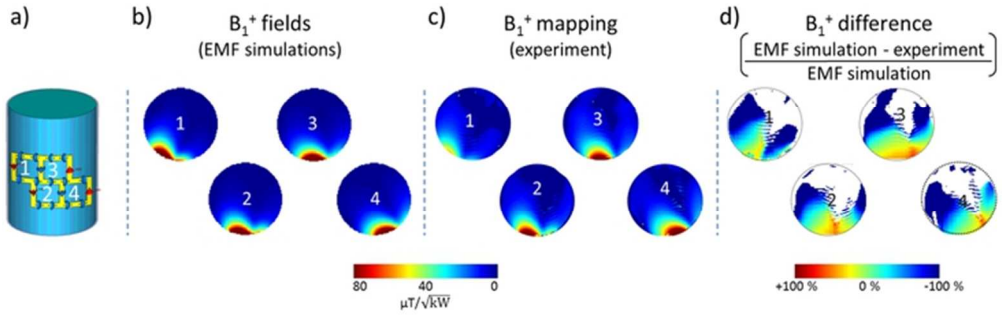

Figure 3:
Example for transmission field assessment with EMF simulations and experimental B_1^+ mapping using a building block equipped with for loop RF elements. For this purpose a cylindrical phantom setup was used in the simulations and in the experiments. a) Virtual model of the setup used for validation (RF shield and casing are not shown but included in the simulations). The experimental setup was arranged analogously to the virtual setup. b) Simulated B_1^+ distribution (absolute values) of four channels which form one curved building block. For B_1^+ evaluation transversal slices through the cylindrical phantom were positioned in alignment with the center of the loop elements. c) Absolute transmission fields derived from B_1^+ mapping of the experimental setup. d) Difference maps in percentage of the simulated results. The results demonstrate the qualitative and quantitative agreement between the numerical simulations and the measurements.
61x19mm (300 x 300 DPI)

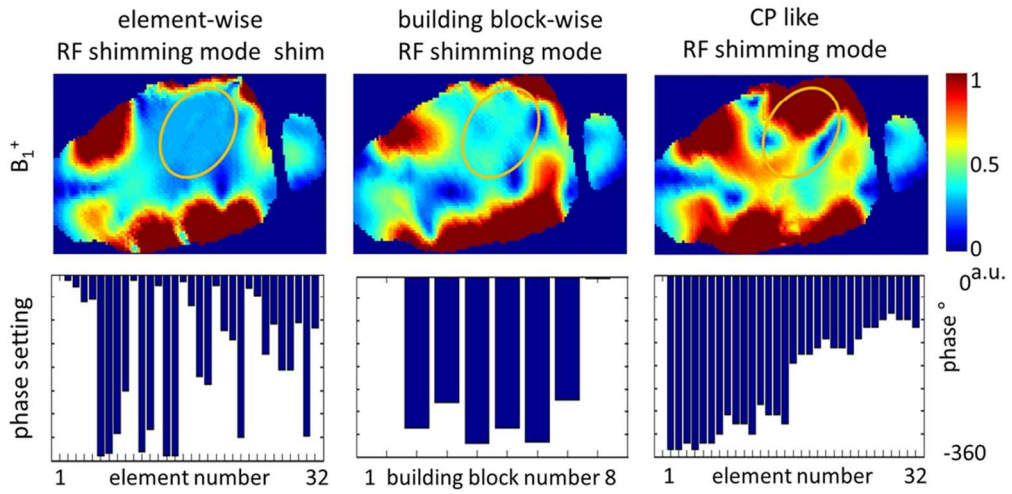

Figure 4:
Transmission field shaping using a 32 channel loop element transceiver array (Figure 1d) (53). In this example of static B_1^+ shimming field shaping is based upon EMF simulations for a multi-oblique plane mimicking a four chamber view of the heart. Top: B_1^+ field distributions for the three phase setting modes including left) an element-wise phase setting approach, center) a block-wise optimized phase setting approach were the phase is set identical for four loop elements forming a 4 channel module and right) a CP like mode. The element-wise phase setting regime provided the most uniform B_1^+ fields across the heart which is marked by the orange ellipse. The building-block wise RF shimming mode provided a more uniform B_1^+ distribution across the four chamber view of the heart versus the CP-like phase setting regime. Bottom: Summary of the phase values used for the three phase setting regimes.
97x47mm (300 x 300 DPI)

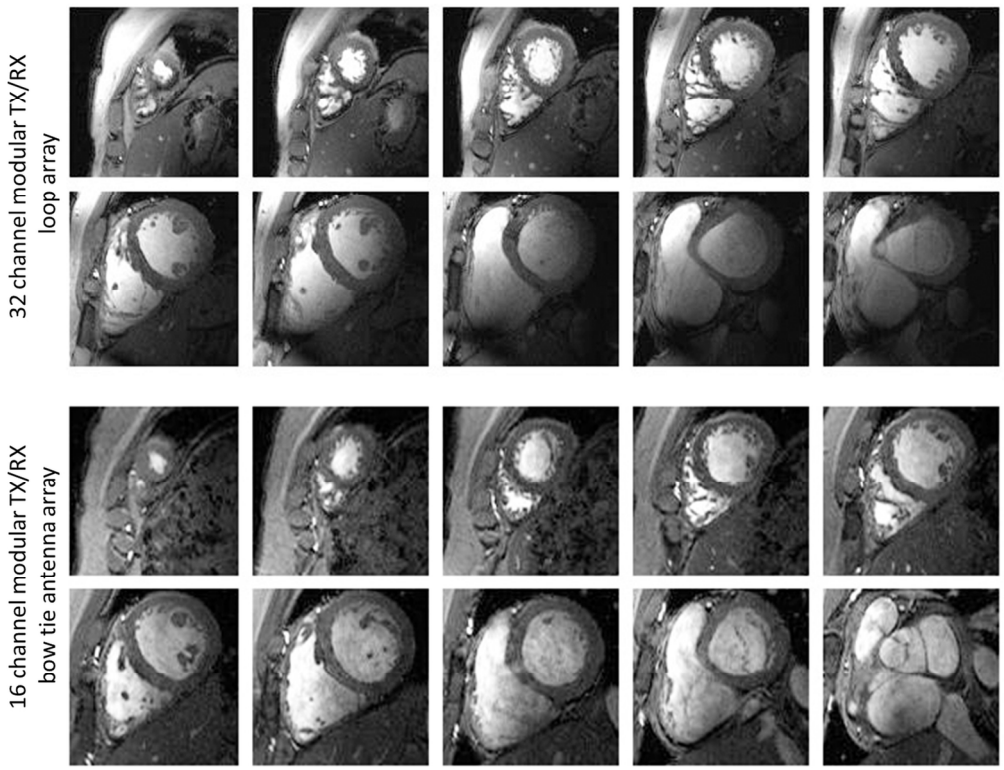

Figure 5:
End-diastolic short axis views covering the heart from the apex to the base derived from 2D CINE FLASH imaging (in-plane resolution (1.1 x 1.1) mm^2, slice thickness 2.5 mm, GRAPPA reduction factor 2,) using top) a 32 channel modular TX/RX loop array and bottom) a 16 channel modular TX/RX bow tie antenna array. Both array configurations provided rather uniform signal intensity and no major signal voids for slices covering the heart from the apex to the base.

152x117mm (300 x 300 DPI)

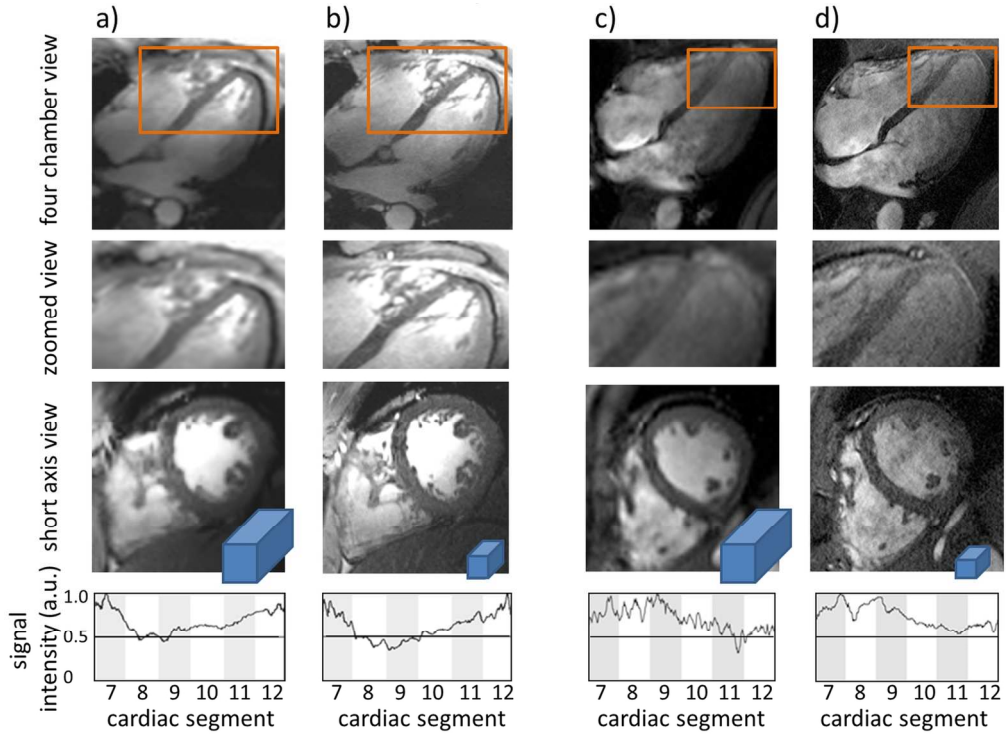

Figure 6:
Four chamber views (1st row) and short axis views (3rd row) of the heart derived from 2D CINE FLASH acquisitions (GRAPPA reduction factor 2) using a,b) a 32 channel modular TX/RX loop element array (Figure 1d) and c,d) a 16 channel modular TX/RX bow tie antenna array (Figure 1f). Different resolution were employed: a,c) standardized clinical protocol: in-plane resolution=(1.8 x 1.8x6.0) mm^3, b) in-plane resolution (1.1 x 1.1x2.5) mm^3 and d) in-plane resolution (0.8 x 0.8x2.5) mm^3. 2nd row: Magnified views of the ventricular trabeculae, demonstrating that spatial resolution enhancements by a factor of six or even twelve versus standardized protocols used in current clinical practice improve the delineation of subtle anatomical details of the heart. Bottom) Analysis of the signal intensity in the short axis view using a profile along a circular trajectory inside the myocardium.

146x107mm (300 x 300 DPI)

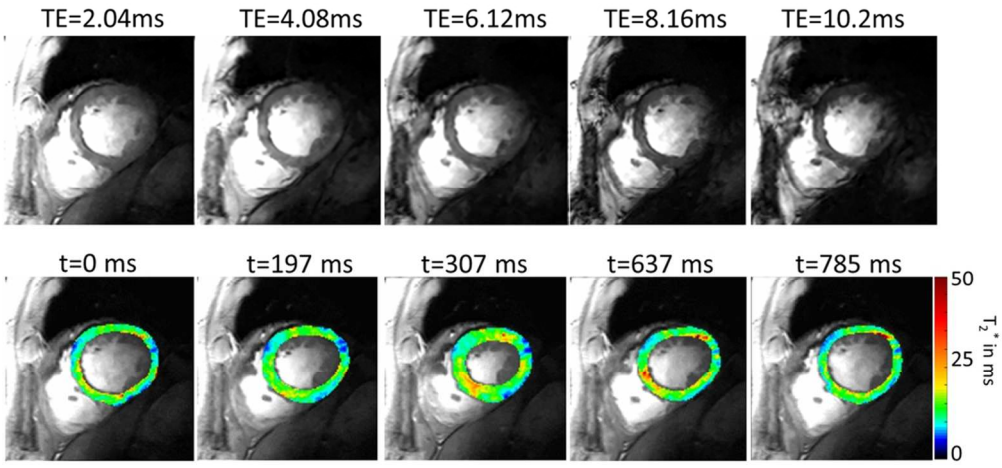

Figure 7:
Example for myocardial T_2* mapping at 7.0 T. Top: T_2* weighted short axis views of the heart for a mid-ventricular slice derived from multi-echo gradient-echo imaging at 7.0 T. Images shown were obtained with echo times of TE=2.04 ms, TE=4.08 ms, TE=6.12 ms, TE=8.16 ms and TE=10.20 ms. A spatially adaptive non-local means (SANLM) denoising filter was applied (191). Bottom: T_2*colour maps of a short axis view of the heart derived from a series of T_2* sensitized 2D CINE acquisitions covering the entire cardiac cycle (5 cardiac phases out of a series of 21 cardiac phases are shown) overlaid to conventional 2D CINE FLASH images.
92x42mm (300 x 300 DPI)

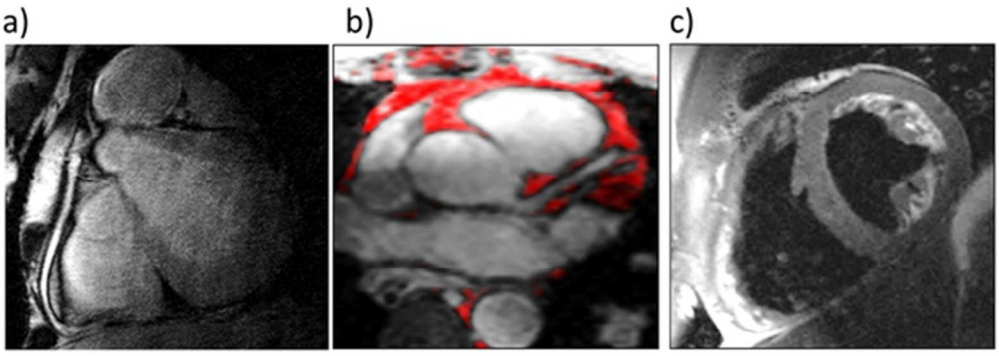

Figure 8:
Examples for emerging UHF-CMR applications: a) high resolution image of the right coronary artery acquired with a spatial resolution of (0.45 x 0.45 x1.2) mm^3 which was facilitated by a navigator gated free breathing 3D gradient-echo acquisition in conjunction with spectrally selective adiabatic inversion recovery at 7.0 T (courtesy of Maurice M. Bizino and Hildo Lamb, Department of Radiology, Leiden University Medical Center, Leiden, The Netherlands). b) fat-water separated (gray scale: water image, colour scale: fat image) coronary artery imaging showing the left main coronary artery using the DIXON approach at 7.0 T. c) black blood imaging of a short axis view of the heart derived from high spatial resolution ((0.9 x 0.9 x 4.0) mm^3) fast spin-echo imaging at 7.0 T.

52x18mm (300 x 300 DPI)

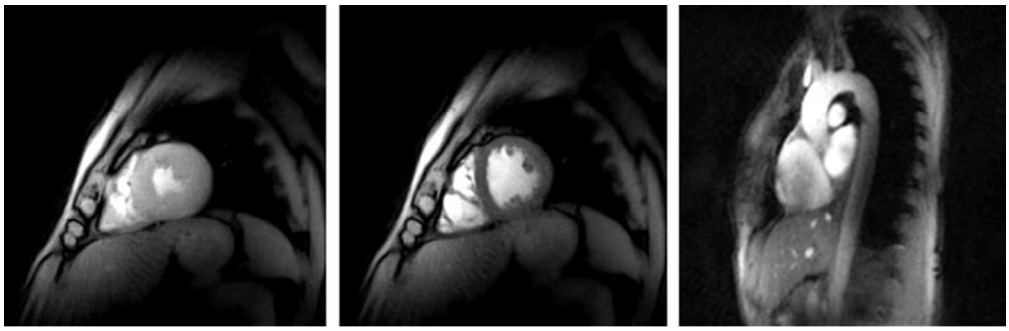

Figure 9:
Examples derived from free breathing real time imaging of a mid-ventricular short axis view of the heart (left: systole, center: diastole) using an 8 channel bow tie antenna array (Figure 1e) and of the aorta (right) using an 16 channel bow tie antenna array (Figure 1f). Images were acquired at a rate of 30 frames per second using highly undersampled radial 2D FLASH with nonlinear inverse reconstruction at a spatial resolution of (1.2 x 1.2 x 6.0) mm^3. The real time images of the aorta demonstrate the 35 cm anatomic coverage of the 16 channel bow tie antenna array along the head-feet direction including details of the liver and the spine without B_1^+ signal voids.

64x20mm (300 x 300 DPI)

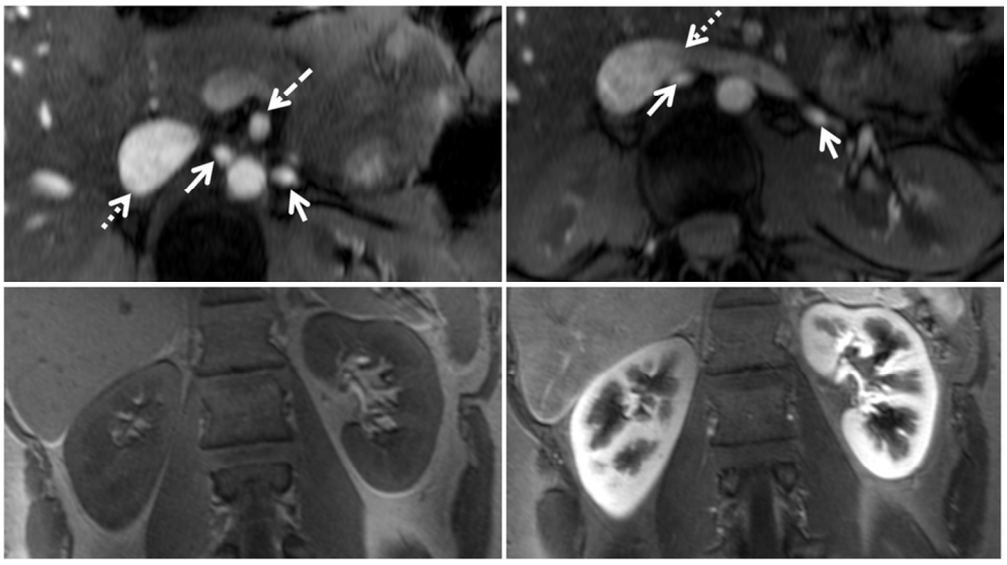

Figure 10:
Examples for renal MRI at 7.0 T. Top: TOF-MRA of the renal vasculature. The arrows point at the proximal (left) and peripheral (right) segments of the renal arteries. The dashed arrow points at the superior mesenteric artery. The dotted arrows demonstrate the venous overlay, by means of the inferior vena cava and left renal vein. Bottom: Non-enhanced (left) and post-contrast (right, 1-M gadobutrol) T1-weighted renal VIBE images. (images courtesy of Lale Umutlu, Erwin L. Hahn Institute for Magnetic Resonance Imaging, University Duisburg-Essen, Essen, Germany)
83x46mm (300 x 300 DPI)

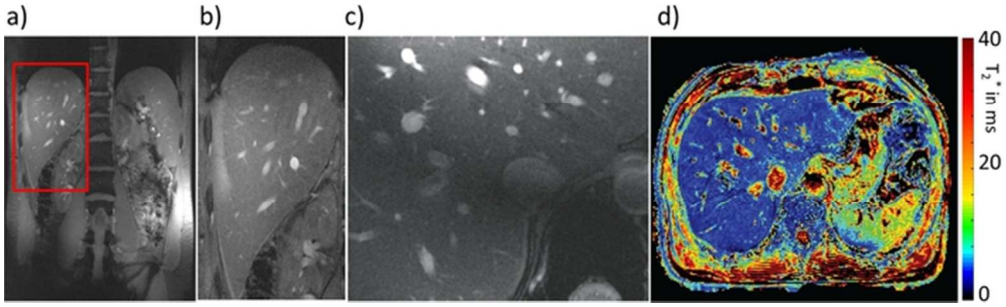

Figure 11:
Examples for liver MRI at 7.0 T. a) T_1 weighted image of a central coronal abdominal slice showing a rather uniform excitation across the liver. The image was derived from gradient-echo imaging using a 32 channel TX/RX loop array (Figure 1d) and a voxel size of (0.4x0.4x2.5) mm^3. b) Zoomed view of the area marked in red in a). c) Zoomed view of a T_1 weighted axial slice covering the liver which was derived from gradient-echo imaging using a 16 channel TX/RX loop array (Figure 1c) and a spatial resolution of (0.3x0.3x2.5) mm^3. No contrast agent was applied. Subtle anatomic liver structures are clearly identifiable including capillaries in the dimension of a diameter of 0.5 mm. d) Abdominal T_2* map showing a rather uniform T_2* distribution across the liver.
59x17mm (300 x 300 DPI)

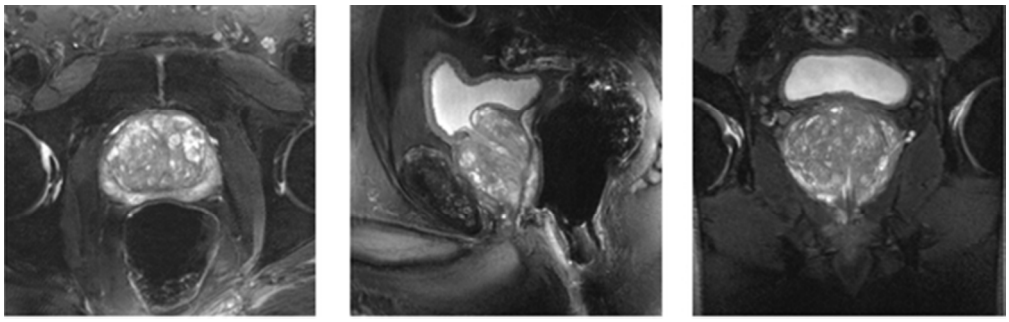

Figure 12:
Axial (left), sagittal (center) and coronal (right) T_2-weighted images of the prostate of a patient (weight 98 kg, age 58 years, PSA 6 ng/ml) at 7.0 T (courtesy of Tom W. J. Scheenen Department of Radiology, Radboud University Medical Centre, Nijmegen, The Netherlands). For data acquisition a fast spin-echo imaging technique was used: TR=3000 ms, TE=71 ms, FOV=(240 x 180) mm^2, matrix 320 x 240, in-plane spatial resolution=(0.75 x 0.75) mm^2, phase encoding direction: anterior-posterior, slice thickness=3 mm, slice gap=0.6 mm, interleaved slice acquisition, 9 echoes, echo spacing 17.8 ms, readout bandwidth 116 Hz/pixel, NA=1, total acquisition time<2 min. To reduce RF power deposition a prolonged 1500 RF pulse as used for refocusing. An 8 channel external stripline array was used for TX/RX and B_1^+-shimming was applied.
46x14mm (300 x 300 DPI)

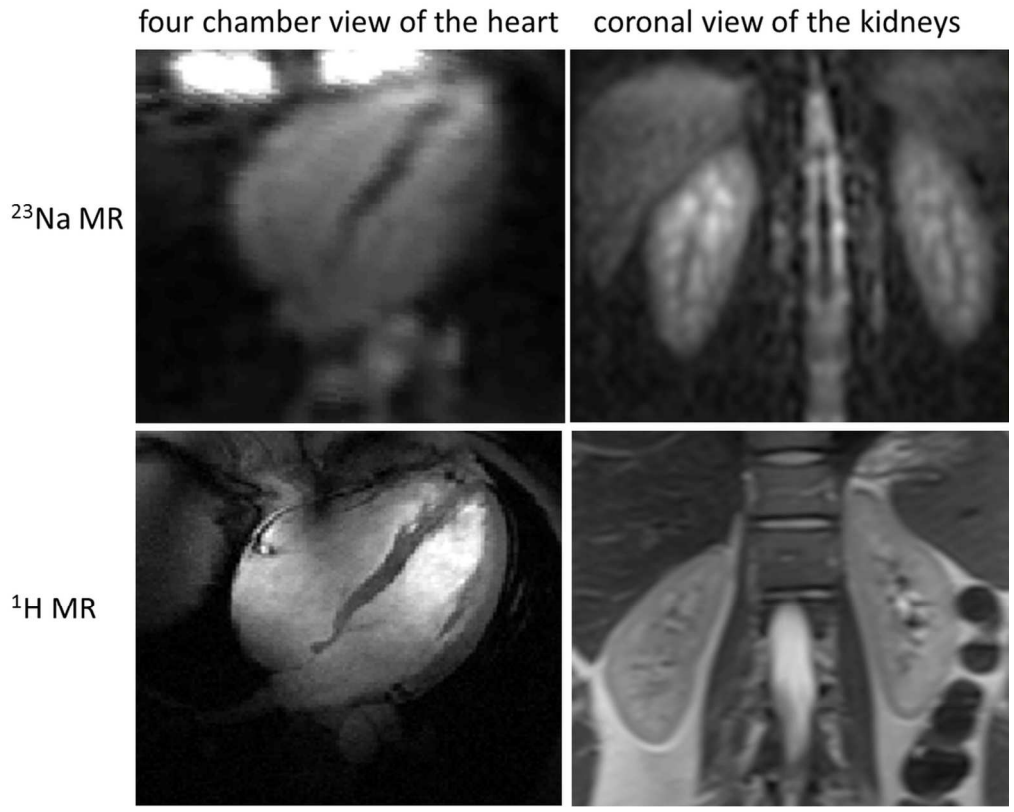

Figure 13:
Top: Sodium images of a four chamber view of the heart (left) and a coronal view of the kidneys (right) acquired at 7.0 T. The ^{23}Na image of the heart was acquired using a density-adapted 3D radial technique (155) with TE= 0.4 ms, TR=11 ms, TRO= 7.1 ms, TX amplitude 115V (~90% SAR) equivalent to a tip angle of 30-40°, number of projections=50000, number of averages=2 and a voxel size of (6 x 6 x 6) mm^3. The ^{23}Na image of the kidneys (courtesy of Stefan Haneder, Institute of Clinical Radiology and Nuclear Medicine, University Medical Center Mannheim, Heidelberg University, Heidelberg, Germany) was acquired with a spatial resolution of (4 x 4 x 5) mm^3 using a 3D Cartesian spoiled gradient-echo sequence with a variable echo time scheme and a highly asymmetric readout (FOV=(256×256) mm^2; matrix size=64×64; number of slices=24; echo time (TE)=4.19 ms; TR=49 ms, total scan time=approximately 40 min). Bottom: 1H four chamber view of the heart (left) derived from 2D CINE gradient-echo imaging at 7.0 T and 1H coronal view of the kidney obtained at 3.0 T (right).

120x96mm (300 x 300 DPI)

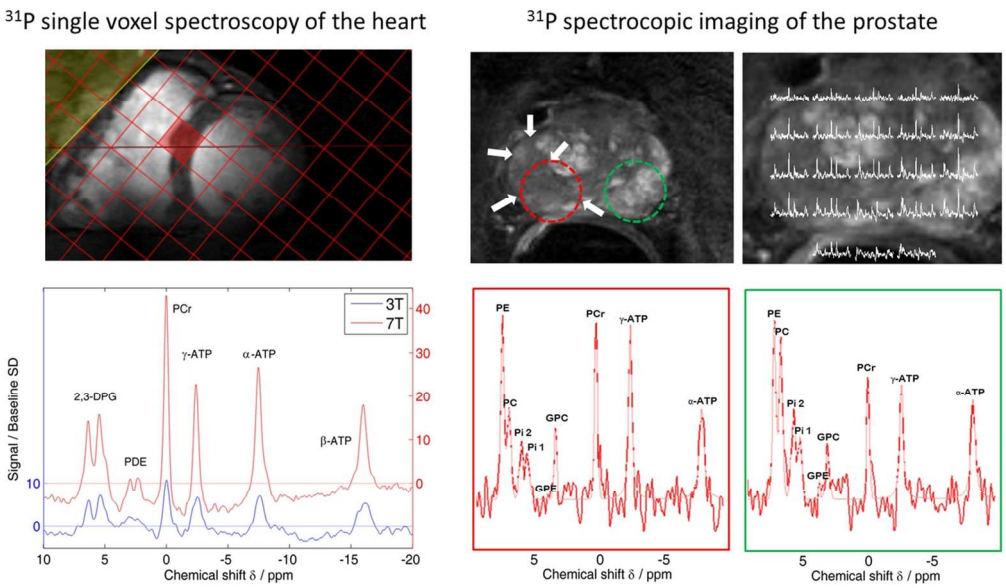

Figure 14:
Examples for ^{31}P MR spectroscopy left) of the heart (courtesy of Christopher Rodgers, Radcliffe Department of Medicine, University of Oxford, Oxford, UK) and right) of the prostate (courtesy of Tom W. J. Scheenen Department of Radiology, Radboud University Medical Centre, Nijmegen, The Netherlands). Left: Comparison of single voxel ^{31}P spectra of the human heart obtained at 3.0T (blue) and at 7.0 T (red). The voxel used for ^{31}P MRS was placed in the middle of the interventricular septum as illustrated in the short axis view of the heart obtained from a 2D CINE FLASH localizer scan at 7.0 T. ^{31}P MRS at 7.0 T provided an SNR advantage over 31P MR spectroscopy at 3.0 T. Right: ^{31}P spectra of a 72-year-old patient with prostate cancer (Gleason score, 4+5; volume, 1.5 cm^3) in the peripheral zone on the right side of the gland. The tumor lesion is indicated by white arrows on the transversal T_2-weighted image. The spectral map shows good quality of ^{31}P spectra across the whole prostate. ^{31}P spectra of the tumor (red circle, red frame) and healthy region (green circle, green frame) are shown separately with the following resonances: phosphoethanolamine (PE), phosphocholine (PC), two phosphate peaks (Pi1 and Pi2), glycerophosphoethanolamine (GPE), glycerophosphocholine (GPC), Phosphocreatine (PCr), gamma-ATP and alpha-ATP. ^{31}P spectra were derived from spectroscopic imaging using a pulse acquire sequence with a 45 degree adiabatic excitation BIR-4 pulse (duration=8 milliseconds), TR=1.5 ms, FOV=(120 x120x120) mm^3; matrix size=10 x10x10, number of averages=12 resulting in voxel volumes of 5.1 cm^3 after apodization with a Hanning filter of the k-space weighted sampling. Total acquisition time was 9 minutes 51 seconds.
116x68mm (300 x 300 DPI)

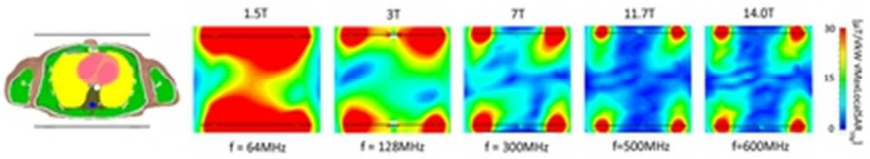

Figure 15:
B_1^+ distribution and RF power deposition derived from EMF simulations at 1.5 T, 3.0 T, 7.0 T, 11.7.0 T and 14.0 T using a four channel TX/RX loop array and the torso of the human voxel model "Duke". For each field strength B_1^+ efficiency distribution is scaled to the maximum local SAR. For each configuration identical phase settings are used for B_1^+ and local SAR (10g average, 1W input power) calculations. The $B_1^+/\sqrt{kW}/\sqrt{(Max(local\ SAR_{10g})}$ distribution is shown for 64 MHz 128 MHz, 300 MHz, 500 MHz and 600 MHz and normalized to an efficiency of $30\mu T/\sqrt{kW}\ \sqrt{(W/kg)}$. B_1^+ uniformity is substantially reduced for the short wave length regime for $B_0 \geq 7.0$ T. For the maximum input power of the coils, which is dictated by MR safety regulations that forbid overriding of maximum local SAR, a lower B_1^+ field is generated while moving from 1.5 T to 14.0 T. This demonstrates that a higher average power is required for the excitation pulse to reach the same flip angle at higher MR frequencies. Given a higher average power and assuming that TR is not prolonged, RF power deposition shows to be significantly enhanced at UHF-MR frequencies ranging between 300 MHz (7.0 T) and 600 MHz (14.0 T).
36x6mm (300 x 300 DPI)

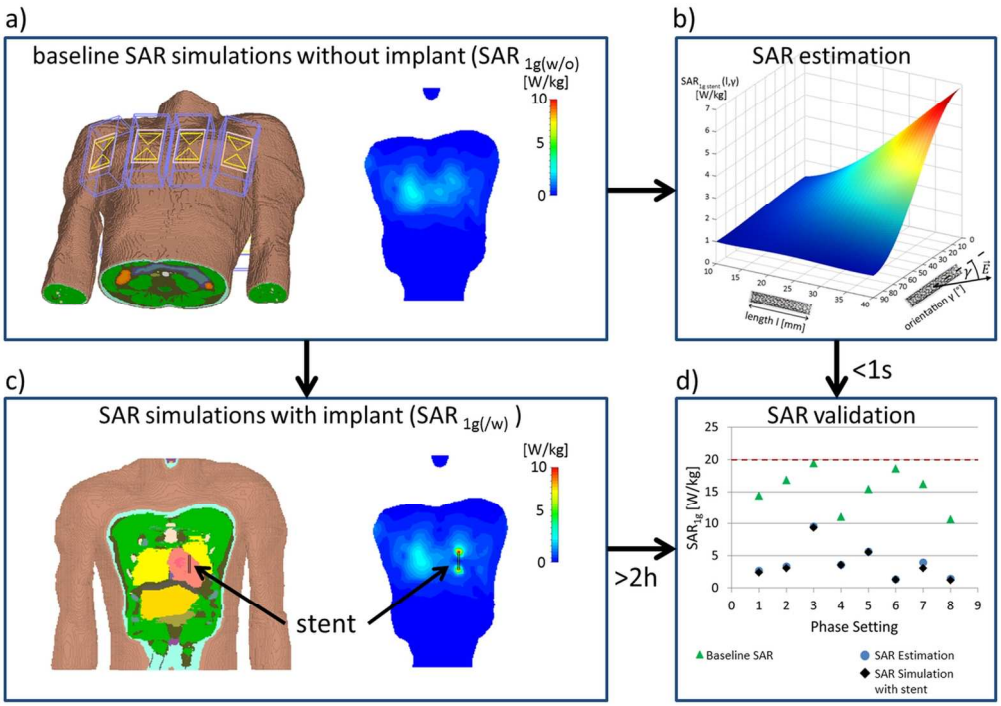

Figure 16:
EMF simulations using the human voxel model „Duke" from the virtual family and an 8 channel transmit/receive bow tie electric dipole array. a) Schematic views of the positioning of the anterior bow tie RF antennas on the anterior chest of the human voxel model and coronal view of SAR_{1g} baseline distribution for a plane through the target position without the stent equivalent being present. b) Surface plot of SAR1g stent derived from equation 2 for baseline SAR_{1g} baseline for an input power of 1W/kg. A stent length ranging from 10-40 mm and a stent rotation versus the main E-field vector ranging from $0\text{-}90^0$ was applied. c) Coronal view of SAR_{1g} stent distribution for a plane through the target position with the stent equivalent being present. d) Simulated maximum baseline SAR1g baseline and SAR1g stent for the stent equivalent using eight randomly generated phase settings compared to the SAR estimation deduced from the analytical approach (equation 2). While conservatively overestimating SAR, SAR estimation using equation 2 was able to predict the induced SAR_{1g} levels without the need to perform extra time consuming EMF simulations with a stent being present in the simulation model.
139x97mm (300 x 300 DPI)